Available online at www.sciencedirect.com
ScienceDirect
Mechatronics 17 (2007) 73–91
MECHATRONICS

Modelling of an automated manual transmission system ☆

Gianluca Lucente, Marcello Montanari *, Carlo Rossi

CASY – Center for Research on Complex Automated Systems "G. Evangelisti", Department of Electronics, Computer and System Sciences (DEIS), University of Bologna, Viale Pepoli 3/2, 40123 Bologna, Italy

Received 21 September 2005; accepted 10 November 2006

Abstract

Vehicles with automated manual transmissions (AMT) for gear shift control offer many advantages in terms of reduction of fuel consumption and improvement of driving comfort and shifting quality. Complexity, nonlinearity and high-order dynamics of the automated driveline, combined with strict requirements for high performance gear shifts, demand the development of driveline models, which include a detailed description of the actuators. These models can be useful for different purposes: (a) during system development, to evaluate the achievable performance and its dependency on system properties; (b) as simulation tools for gear shift control algorithm design. In this paper, physically-based detailed nonlinear models of the electro-hydraulic actuated gearbox and of the dry clutch electro-hydraulic actuator of an automated manual transmission are developed. In order to analyze their behavior and their impact on the drivetrain during gear shifts, actuator models are integrated with a simplified transmission shafts dynamics. A reduced-order model of the gearbox actuator, which is valid when dither signal is imposed to servovalves, is developed with the aim of analyzing its properties and performances.

Model parameter identification has been performed mostly by means of theoretical relations and design data. Experimental tests, performed on a commercial car, confirm that the proposed model is able to describe the actuators behavior and the main phenomena characterizing system dynamics during gear shift.

Keywords: Automated manual transmission; Modelling; Automotive; Electro-hydraulic systems; Singular perturbation method

1. Introduction

Automatic transmission control represents one of the key elements for the improvement of vehicle safety, comfort, reliability and driving performances together with the reduction of fuel consumption and emissions in modern vehicles [1]. Different approaches, such as automatic, continuously variable and automated manual transmission, have been pursued [2,3,4]. The AMT, exploiting the availability of reliable drive-by-wire technologies, represents an important solution for the automotive industry and is spreading in the last years, mostly in the European car market.

An AMT is generally constituted by a dry clutch and a multi-speed gearbox, both equipped with electro-mechanical or electro-hydraulic actuators, which are driven by an Electronic Control Unit (ECU). This paper focuses on an electro-hydraulic actuated system, which is the most frequent solution thanks to its lower weight and the possibility of integrating the actuators with existing hydraulic equipments. The operating modes of AMTs are usually two: semi-automatic, with the driver requesting a sequential gear shift by means of a proper interface, or fully automatic. In both cases, after the gear shift request, the ECU takes the control of the shifting strategy, by issuing suitable command signals to the engine, the dry clutch and the gearbox, according to current engine regime, driving conditions and driving mode, e.g. economical or sport profile.

☆ This paper was not presented at any IFAC meeting.

* Corresponding author. Tel.: +39 0 512093874; fax: +39 0 512093871.
E-mail addresses: glucente@deis.unibo.it (G. Lucente), mmontanari@deis.unibo.it (M. Montanari), crossi@deis.unibo.it (C. Rossi).

0957-4158/$ - see front matter © 2006 Elsevier Ltd. All rights reserved.
doi:10.1016/j.mechatronics.2006.11.002

With respect to manual transmission, the AMT allows to improve driving comfort and shift quality (minimum shifting time decreases from 0.3 s with manual transmission to 0.1 s with AMT). For market sectors such as large-series and ecological cars, AMT has the advantage of lower weight and higher efficiency with respect to other typologies of automatic transmissions. Moreover, since AMT is directly derived from manual transmission with the integration of servo-actuators into existing devices, development and production costs are generally lower than other automatic transmissions. Furthermore, for high class sport cars, vehicle dynamic performances and driving quality can be strongly improved with respect to automatic transmissions. It is worth to point out that one of the limitations of the AMT could be driving comfort reduction, caused by lack of traction during gear shift actuation. However, this drawback is not due to intrinsic limitations of the AMT, but it can be solved by proper gear shift management.

An overall strategy aiming to the improvement of the gear shift quality should take into account the reduction of shifting time, the minimization of mean vehicle deceleration due to traction loss and the minimization of vehicle and driveline oscillations due to variation of transmitted torque. Since the overall performance of the gear shift is highly influenced by all the components involved in the AMT, a detailed model of the driveline for AMTs is useful both during the drivetrain system development/design phases and for gear shift control algorithm design.

Many researches on AMT drivetrain modelling and control have been carried out. In [5] a detailed model for the analysis of the driveline torsional vibrations has been developed. Transmission shafts have been modelled by means of finite element technique, and dry clutch nonlinear characteristic and gearbox backlash have been taken into account. For the same purpose, in [6] a high-order nonlinear model based on multi-body model formulation has been developed for a driveline with manual transmission.

Detailed models of clutch electro-hydraulic and electromechanical actuators for AMT have been described in [7,8], in order to derive algorithms for actuator control.

In studies devoted to gear shift control [9,10,11,12], reduced-order driveline models have been usually considered, and clutch and gearbox actuator dynamics have been described by simple models or have been neglected. In [10,13] two different models describing the torsional behaviour of the driveline during engaged and neutral phases have been developed. Linear models have been derived considering equivalent lumped inertias for engine, gearbox and wheels and one torsional flexibility for the secondary shaft. The same approach has been followed in [14] to model the clutch slipping and locked phases. It is worth to note that in both modelling- and control-oriented papers the effects of actuators have not been taken into account. Nevertheless, actuator dynamics cannot be neglected at all, since it can considerably affect shifting performances, mainly when fast and high comfort maneuvers are required.

In this paper, physically-based nonlinear models of the electro-hydraulic gearbox and clutch actuators are developed in a detailed way. Since actuator dynamics are highly interconnected to the driveline dynamics, it is necessary to combine them with a drivetrain model, for model validation and analysis of gear shift operations. Hence, an overall driveline model is derived, by combining the actuator models with a simplified but sufficiently accurate model of the transmission shafts. According to previous considerations, the objectives of the modelling process are twofold. First, the proposed model accurately describes the dynamics of the servo actuated clutch and gearbox and allows to analyze the influence of servo actuators (and their components) on the driveline behaviour and on gear shift performances. Moreover, the proposed simulation model represents one of the key issues for the design and evaluation of gear shift control strategies. With respect to previous works, the main feature of this paper is that it focuses on the actuator dynamics and their integration into the overall system, thus providing a model which can be useful for the design of high performance gear shift controllers.

The pursued modelling approach decomposes the driveline into three main subsystems: transmission shafts and electro-hydraulic gearbox and clutch. In Figs. 1 and 2 a sketch of the driveline and a schematic block diagram of the overall model are shown. In this paper, the main focus is devoted to modelling of the servo-actuated clutch and gearbox.

In Sections 2.1–2.3 the gearbox actuator is modelled by decomposition into a hydro-mechanical actuator used for speed selection, pressure control servovalves and connecting pipelines. The high-order, highly nonlinear model takes into account the electromagnetic, hydraulic and mechanical dynamics of the actuator. Based on this detailed model, a reduced-order model of the hydraulic gearbox actuator is derived applying singular perturbation and averaging theories in Section 2.4. For model reduction the presence of dither is exploited to smooth the nonlinearity coming from Bernoulli's equation combined with the servovalve dead-zone. This model allows to get insight on system properties, such as frequency analysis of the linearized model.

The clutch actuator model, describing the dynamic relation between applied pressure on the clutch piston and transmissible clutch torque, is addressed in Section 3. It represents a refinement of the model developed by the authors in [7], where the focus was on the electro-hydraulic dynamics.

In Section 4 actuator models are combined with the dynamics of the transmission shafts connecting the engine to the wheels. In this way, by exploiting a hybrid system formalism, an overall model describing how engine torque, clutch disk position and gearbox actuator configuration act on shaft and wheel speeds during gear shift is developed.

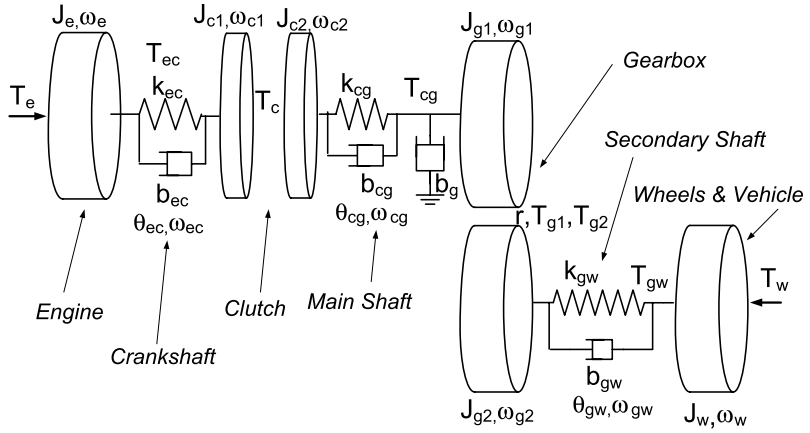

Fig. 1. Sketch of the driveline.

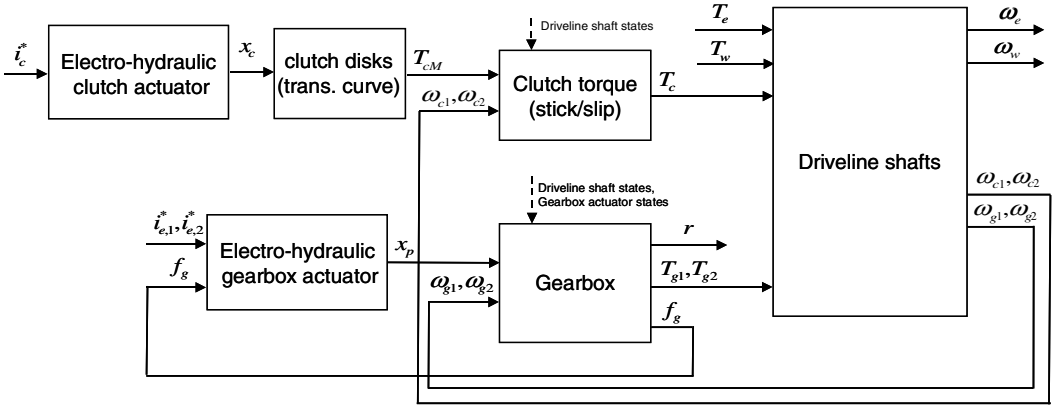

Fig. 2. Block diagram of the driveline model.

Preliminary results on the overall driveline model have been presented by the authors in [15].

Parameter identification and model validation based on experimental tests are presented and discussed. Experimental tests and detailed analysis of the steady-state and dynamical properties of the gearbox actuator are presented in Section 5.1, while in Section 5.2 the overall model is validated on experimental results relative to standard gear shifts. Conclusions are drawn in Section 6. Nomenclature used through the rest of the paper is reported in Appendix B.

2. Gearbox actuator model

In the considered servo-actuated six-speeds indirect gearbox, selection of the gear ratio is performed by locking a particular couple of cogwheels to the shafts by means of a two-degree-of-freedom electro-hydraulic actuator. It is capable of both rotating the gearbox fork to perform the selection of one of the three ranks and translating it for the engagement of even or odd speeds within the same rank. In this section, the model of the actuator for gear engagement, which is schematically shown in Fig. 3, is

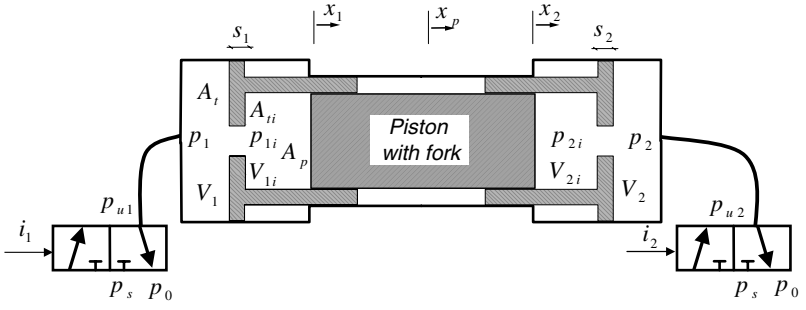

Fig. 3. Schematic diagram of the actuator for gear engagement. When $x_p = 0$, piston is in the middle position. When $x_1 = 0$, $x_2 = 0$ left and right tappets are at the internal stops respectively.

derived. Gearbox actuator is interconnected to the main and secondary shaft dynamics through speeds ω_{g1}, ω_{g2} (output variables for the shaft subsystem) and transmitted torques T_{g1}, T_{g2} (input variables), which depend on the gearbox operating condition (see Figs. 1 and 2). The electro-hydraulic actuator is decomposed into three main subsystems: hydraulic actuator, servovalves and pipelines. Servovalve and pipeline models are the same for both the hydraulic circuits, denoted by lowerscripts 1,2.

2.1. Hydraulic actuator

The actuator (see also Fig. 3) is composed by a piston joined with a fork acting on the cogwheels. Left and right positions correspond to engaged odd and even gears respectively, while the middle position corresponds to neutral. Opposite axial forces can be applied by means of two distinct hydraulic circuits, controlled by two single-stage pressure control valves connected to the actuator by two long flexible pipelines. The motion of the piston is determined by two tappets, whose stroke is limited by mechanical constraints. The latter ones allow to stop the tappets and the piston into positions with engaged odd and even speeds or into the neutral position. The tappets guarantee that the piston moves to the middle position when equal pressures are applied, due to modification of the effective areas on the two sides of the piston: in fact, when a tappet is in contact with the piston, the effective area on the corresponding side is greater than the other one. Note that, in order to keep the fork in a certain position, e.g. with engaged gear, no force is required to be applied to the piston.

The actuator model consists of the mechanical dynamics of the tappets and the piston and the hydraulic dynamics of the outer and inner chambers. The actuator volume can be divided into four chambers by the tappets and the piston: outer chambers, with pressures p_1, p_2 acting on the tappets, are directly connected to the pipelines, while inner chambers have pressures $p_{1,i}$, $p_{2,i}$ acting both on the tappet and the piston. Pressures $p_{1,i}$, $p_{2,i}$ act on an effective area lower than that of pressures p_1, p_2 and with opposing effect. An orifice connects the inner and outer chamber on each side of the actuator.

Considering tappets and piston positions delimited by constraints $x_1 \in [\bar{x}_1, 0]$, $x_p \in [x_1, x_2]$ and $x_2 \in [0, \bar{x}_2]$, chamber volumes change depending on the position of the tappets and the piston as

$$
\begin{aligned}
V_1 &= V_{10} + A_1 x_1,\\
V_{1,i} &= V_{1,i0} + A_{1,i}(x_p - x_1),\\
V_2 &= V_{20} - A_2 x_2,\\
V_{2,i} &= V_{2,i0} + A_{2,i}(-x_p + x_2).
\end{aligned}
$$

Note that, from relations between constraints, the piston cannot be in contact with two tappets simultaneously, apart in the middle position ($x_1 = x_p = x_2 = 0$).

Assuming laminar oil flow [16, Chapter 3] through the orifices $q_{k,i} = g_{od}(p_k - p_{k,i})$, $k = 1,2$, pressure dynamics are given by the fluid continuity equations

$$
\begin{aligned}
\dot{p}_1 &= \frac{\beta}{V_1}\left[q_1 - q_{1,i} - A_1 v_1\right],\\
\dot{p}_2 &= \frac{\beta}{V_2}\left[q_2 - q_{2,i} + A_2 v_2\right],\\
\dot{p}_{1,i} &= \frac{\beta}{V_{1,i}}\left[q_{1,i} - A_{1,i}(v_p - v_1)\right],\\
\dot{p}_{2,i} &= \frac{\beta}{V_{2,i}}\left[q_{2,i} - A_{2,i}(v_2 - v_p)\right].
\end{aligned}
$$

Tappets and piston mechanical dynamics are described by the following equations

$$
\begin{aligned}
&\dot{x}_p = v_p,\\
&\dot{v}_p = \frac{1}{m_p}\left[A_p(p_{1,i} - p_{2,i}) - b_{vp} v_p + \lambda_{1p} - \lambda_{2p} + f_g\right],\\
&\dot{x}_1 = v_1,\\
&\dot{v}_1 = \frac{1}{m_1}\left[A_t p_1 - A_{t,i} p_{1,i} - b_{v1} v_1 - \lambda_{1i} + \lambda_{1e} - \lambda_{1p}\right],\\
&\dot{x}_2 = v_2,\\
&\dot{v}_2 = \frac{1}{m_2}\left[A_{t,i} p_{2,i} - A_t p_2 - b_{v2} v_2 - \lambda_{2e} + \lambda_{2i} + \lambda_{2p}\right],\\
&0 \leqslant (x_p - x_1) \perp \lambda_{1p} \geqslant 0,\\
&0 \leqslant (x_2 - x_p) \perp \lambda_{2p} \geqslant 0,\\
&0 \leqslant -x_1 \perp \lambda_{1i} \geqslant 0,\\
&0 \leqslant (x_1 - \bar{x}_1) \perp \lambda_{1e} \geqslant 0,\\
&0 \leqslant x_2 \perp \lambda_{2i} \geqslant 0,\\
&0 \leqslant (\bar{x}_2 - x_2) \perp \lambda_{2e} \geqslant 0,
\end{aligned}
\tag{1}
$$

where unilateral constraint forces, denoted by λ_{ki}, λ_{ke}, λ_{kp}, with $k = 1, 2$, represent the forces exerted by the stops on the tappets and between tappets and piston.

Remark 2.1. In order to express these forces depending on whether or not the stop is active, the "complementarity" condition "$0 \leqslant x \perp \lambda \geqslant 0$", which stands for $x \geqslant 0$, $\lambda \geqslant 0$ and $x \cdot \lambda = 0$, is used [17]. It is worth noting that the displacement with respect to the stop necessarily satisfies $x \geqslant 0$, while it holds $\lambda \geqslant 0$, since the force exerted by the stop can act in one way only. In the hybrid system framework, each constraint defines two modes: the unconstrained one, with $x \geqslant 0$ and $\lambda = 0$ (stop is not active), and the constrained one, with $x = 0$ and $\lambda \geqslant 0$. In this case, expression of the generic constraint force λ can be determined imposing x with its 1st and 2nd time derivatives equal to zero in the corresponding dynamical equations in (1). Expressions of λ_{ki}, λ_{ke}, λ_{kp}, with $k = 1, 2$ in the various modes are not reported here for the sake of space.

Violation of inequalities $x \geqslant 0$, $\lambda \geqslant 0$ leads to mode transitions. In (1), denoting with x^+ the right-hand limit of x at the event time when transition takes place, and supposing that impacts are inelastic, i.e. no bounce occurs, reset of continuous variables is performed according to the following jump rules:

$$\begin{aligned}
v_p^+ = v_1^+ &= \frac{m_1 v_1 + m_p v_p}{m_1 + m_p} && \text{if } x_p = x_1, v_p < v_1,\\
v_p^+ = v_2^+ &= \frac{m_2 v_2 + m_p v_p}{m_2 + m_p} && \text{if } x_2 = x_p, v_2 < v_p,\\
v_1^+ &= 0 && \text{if } x_1 = 0, v_1 > 0,\\
v_1^+ &= 0 && \text{if } x_1 = \bar{x}_1, v_1 < 0,\\
v_2^+ &= 0 && \text{if } x_2 = 0, v_2 < 0,\\
v_2^+ &= 0 && \text{if } x_2 = \bar{x}_2, v_2 > 0.
\end{aligned} \tag{2}$$

In (1) external force f_g represents the reaction force applied on the piston by gearbox devices acting on the cogwheels, during gear engaging and disengaging phases. Expressions of f_g, T_{g1}, T_{g2} and gear ratio r depend on gearbox operations and shaft torque/speed, as defined by the automaton relative to the 1st and 2nd gears depicted in Fig. 4. Piston displacements relative to disengaging and synchronization phases are related by $\bar{x}_1 \leqslant x_{D1} \leqslant x_{S1} \leqslant 0 \leqslant x_{S2} \leqslant x_{D2} \leqslant \bar{x}_2$.

Consider the 1st to 2nd gear shift (2nd to 1st gear shift is similar, and the automaton can be simply extended to other speeds). When the first gear is engaged (state Engaged_1, $r = r_1$), the piston is on the left, i.e. $\bar{x}_1 \leqslant x_1 \leqslant x_p \leqslant x_{D1}$, it holds $\omega_{g1} = r_1 \omega_{g2}$ and transmitted torques are $T_{g1} = T_g^*$, $T_{g2} = r_1 T_g^*$, where T_g^*, whose expression will be defined in Section 4, is the torque such that gear engagement is kept ($\dot{\omega}_{g1} = r_1 \dot{\omega}_{g2}$).

In order to enter neutral phase, the piston is moved toward the middle position by applying pressure p_1. Disengagement (state Disengagement_1) starts at $x_p = x_{D1}$, where the piston stops, until transmitted torque T_g^* decreases under a threshold dependent on f_g. In fact, constraint force $f_g = f_{g1}^*$ acting on the piston in this state can be thought as the stiction force opposing disengaging (and hence piston movement) and whose maximum amplitude is proportional to transmitted torque. Expressions of f_{g1}^* and f_{g2}^* during disengagement are such that x_p remains constant. Supposing that one tappet is joined with the piston during disengagement and synchronization phases, while the other is not in contact, they are obtained from (1) imposing constant x_p as

$$f_{g1}^* = -(A_p - A_{t,i}) p_{1,i} - A_t p_1 + A_p p_{2,i},$$
$$f_{g2}^* = (A_p - A_{t,i}) p_{2,i} + A_t p_2 - A_p p_{1,i}.$$

When transmitted torque decreases, i.e. when $|f_g| \geqslant k_{gD}|T_g^*|$, cogwheels can disengage, and gearbox enters in neutral (state Neutral), where no external force is applied to the piston ($f_g = 0$) and transmitted torque between gearbox shafts T_{g1}, T_{g2} is null. During this phase, gearbox rank selection can be performed if needed. In order to engage the 2nd gear, synchronization phase (state Synchro_2) is first performed by applying pressure p_1 to the piston. The piston stops at $x_p = x_{S2}$, where the synchronizer starts working. In fact, gear engaging is possible only when main and secondary shaft speeds are related by the correct gear ratio r_2. The synchronizer is modelled as a device which

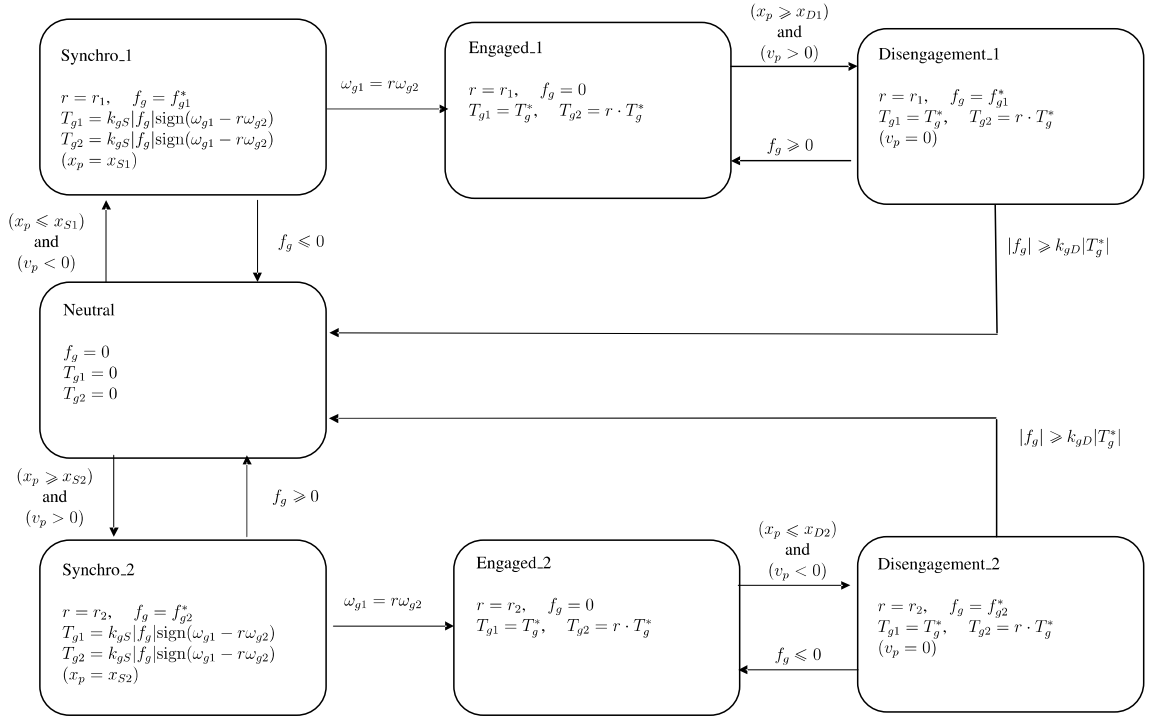

Fig. 4. Representation of the finite state automaton for 1st and 2nd gears.

applies Coulomb friction torque to the cogwheels, thus dissipating the exceeding kinetic energy of gearbox shafts on two conic surfaces. Torque amplitude $T_{g1} = T_{g2}$ is proportional to normal force f_g applied to the gearbox fork, which is also related to pressure applied to the piston. Hence, force $f_g = f_{g2}^*$ can be thought as a reaction force which opposes the piston movement. When the cogwheels engage ($\omega_{g1} = r_2\omega_{g2}$), force f_g becomes null and the piston moves to the right position (state Engaged_2, with $x_p \geqslant x_{D2} \geqslant x_2 \geqslant \bar{x}_2$), where transmitted torques $T_{g1} = T_g^*, T_{g2} = r_2 T_g^*$ are such that gear engagement is kept.

2.2. Pressure control valve

A sketch of the two single-stage pressure control valves [16] for gear engagement is shown in Fig. 5. Main feature of pressure control valve is that it is a closed-loop control system: pressure feedback is determined by an internal "sensing" chamber connected by a capillary to the user port, which provides a feedback force proportional to the user pressure acting on the valve plunger.

The servovalve model, composed by the mass-spring-damper dynamics of the plunger and by the electro-magnetic dynamics, is given by

$$\begin{aligned}
\dot{x}_v &= v_v,\\
\dot{v}_v &= \frac{1}{m_v}[f_e - k_v x_v + f_{v0} - b_v(v_v) + F_b(x_v, p_u, p_s, p_0) - A_c p_c],\\
\dot{f}_e &= -\frac{1}{\tau_e} f_e + \frac{1}{\tau_e} k_f |i_e^*|,
\end{aligned} \tag{3}$$

where $F_b = 2n_o c_{db}\,[A_d(x_v)(p_u - p_0) - A_f(x_v)(p_s - p_u)]$ is the steady-state Bernoulli force [16, Chapter 5], which is present with non null oil flow and acts as a disturbance opposing to the opening of the orifices. In (3), f_e is the force applied on the plunger by a linear variable reluctance machine. More details on the electro-magnetic model of the servovalve can be found in [7]. Since it results that the steady-state value of f_e is approximatively proportional to the coil current, and taking into account the servovalve current driver and the electro-magnetic coil dynamics, a linear first-order filter with time constant τ_e between command current i_e^* and force f_e has been introduced to model the current-controlled electrical machine.

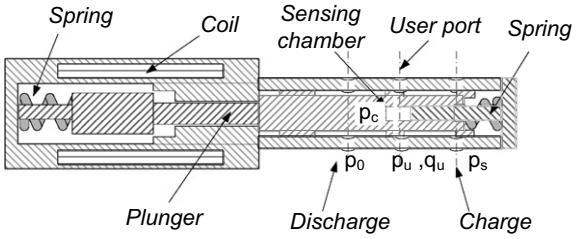

Fig. 5. Schematic diagram of the pressure control valve.

The sensing chamber pressure dynamics is given by

$$\begin{aligned}
\dot{p}_c &= \frac{\beta}{V_{c0} - A_{c0}x_v}(q_{oc} + A_{c0}v_v),\\
q_{oc} &= g_c(p_u - p_c),
\end{aligned} \tag{4}$$

where $g_c = n_{oc}\frac{\pi r_{oc}^4}{8\mu l_{oc}}$ and Poiseuille law for laminar flow q_{oc} through the capillary tubes connecting the sensing chamber to the user port has been utilized [16, Chapter 3].

Oil flow q_u at the user port depends on the plunger position, which determines if the user port is connected to the low pressure tank (dumping), to the high pressure supply (filling) or it is in the dead-zone, since the valve is overlapped. The oil flow is expressed by Bernoulli's equation

$$q_u(x_v, p_u) = \begin{cases} -n_o c_d \sqrt{\dfrac{2}{\rho}}\sqrt{p_u - p_0}\cdot A_d(x_v) & \text{if } x_v \leqslant x_{vd},\\ 0 & \text{if } x_{vd} \leqslant x_v \leqslant x_{vf},\\ n_o c_d \sqrt{\dfrac{2}{\rho}}\sqrt{p_s - p_u}\cdot A_f(x_v) & \text{if } x_v \geqslant x_{vf}. \end{cases} \tag{5}$$

The low pressure circuit is constituted by a tank at atmospheric pressure, hence it can be assumed that $p_0 \cong 0$ bar, while a sufficiently large accumulator at high pressure, filled by a pump, provides an (almost) constant pressure $p_s \cong 50$ bar. It is assumed that $p_0 \leqslant p_u(t) \leqslant p_s$, $\forall t$.

Remark 2.2. A conceptual scheme of the servovalve model is depicted in Fig. 6. It is worth noting that, considering $V_{c0} \gg A_{c0}x_v$ and $q_{oc} \gg A_{c0}v_v$ in (4), the pressure p_c is the linear first-order filtering of the user pressure p_u. From (3)–(5), it follows that the servovalve can be considered as a closed-loop system with negative feedback, thanks to the

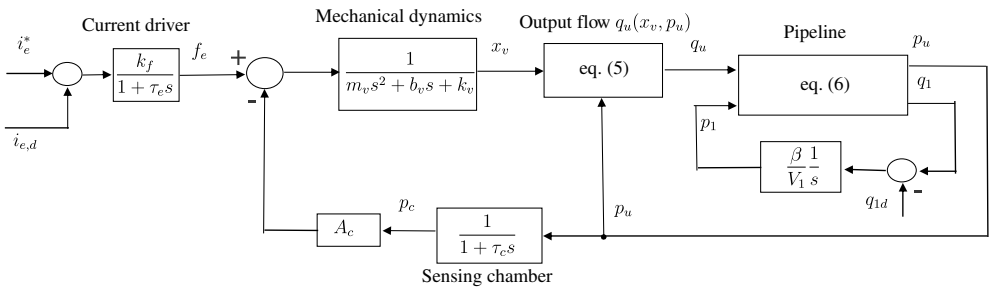

Fig. 6. Conceptual scheme of the pressure control valve connected to the pipeline and the gearbox actuator. $i_{e,d}$ stands for the dither signal, q_{1d} for speed-dependent oil-flow disturbance.

sensing chamber pressure acting on the plunger. In steady-state conditions and supposing a capacitive load, when constant current i_e^* is applied, spring, electrical and sensing pressure forces are balanced, yielding to proportionality between command current and user pressure. In this condition, the plunger is in the dead-zone, and no oil flows through the valve. Dynamical properties of the mechanical and hydraulic model of the pressure control valve will be investigated in next sections.

2.3. Pipeline

Due to vehicle layout constraints, pressure control valves are connected to the hydraulic actuator through flexible and long (0.7 m) pipelines. In order to model the line, the dissipative modal approximation technique is adopted. A linear friction model with correction terms introduced to compensate for frequency-dependent viscosity is considered, as in [18,19,7]. By means of harmonic analysis of the pipeline and mechanical and hydraulic loads, it can be concluded that, for the considered modelling purposes, the fundamental mode is sufficient to approximate the finite delay terms introduced by the pipeline [18]. Hence, the pipeline is modelled as a 2-port system with input/output variables given by the servovalve and the actuator oil flows and pressures. It is expressed in state-space form by the following R-L-C dynamics:

$$\begin{bmatrix} C_p\dot{p}_u \\ L_p\dot{q}_1 \end{bmatrix} = \begin{bmatrix} 0 & -\frac{\pi}{2} \\ \frac{\pi}{2}\frac{1}{\alpha_p^2} & -\frac{R_p\beta_p}{\alpha_p} \end{bmatrix} \begin{bmatrix} p_u \\ q_1 \end{bmatrix} + \begin{bmatrix} 0 & \frac{\pi}{2} \\ -\frac{\pi}{2}\frac{1}{\alpha_p^2} & \frac{R_p\beta_p}{\alpha_p} - \frac{4Z_0D_n\pi}{\alpha_p^2} \end{bmatrix} \begin{bmatrix} p_1 \\ q_u \end{bmatrix} \quad (6)$$

where the hydraulic parameters are defined as $C_p = \frac{l_pA_p}{\rho c_p^2}$, $L_p = \frac{\rho l_p}{A_p}$, $R_p = \frac{8\rho\nu l_p}{A_p r_p^2}$, $c_p = \sqrt{\frac{\beta_{e,p}}{\rho}}$, $Z_0 = \frac{\rho c_p}{A_p}$, $D_n = \frac{l_p\nu}{c_p r_p^2}$ and α_p, β_p are correction terms to take into account frequency-dependent viscosity [18].

2.4. Reduced-order model of the gearbox actuator

In this section, the steady-state characteristic of the pressure control servovalve is analyzed. Then, a reduced-order model of the gearbox actuator is derived, under assumption of application of dither signal to the command current and exploiting singular perturbation and averaging theories. Based on this model, the frequency response analysis is carried out.

2.4.1. Pressure control valve steady-state characteristic

In Fig. 7 simulated and experimental pressure vs current steady-state characteristics of the pressure control valve are shown. They have been determined by applying a (slowly variable) command current profile with constant slope

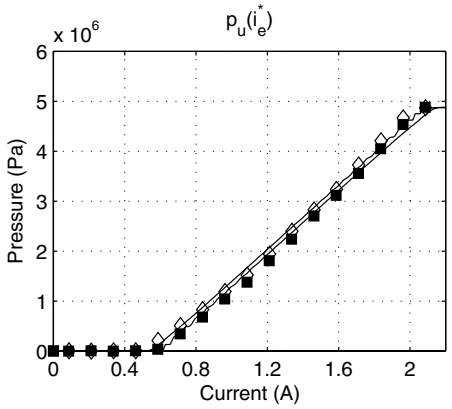

Fig. 7. Servovalve pressure vs current steady-state characteristic. Simulation (solid) and experimental data: rising current (black mark), falling current (white mark).

± 0.1 A/s, starting from 0 A to 2.2 A and back, lasting 44 s. For currents lower than $i_0 = \frac{k_v x_{vf} - f_{v0}}{k_f} \cong 0.6$ A the valve plunger remains in the dumping region, hence no oil flows at the user port and p_u is null. For currents greater than i_0, the steady-state characteristic is almost linear and can be obtained from the servovalve model (3),(4) at the equilibrium as

$$p_u = \frac{1}{A_c}(k_f|i_e^*| - k_v x_v' + f_{v0}) \quad (7)$$

with $x_v' = x_{vf}$ during positive slope phase and $x_v' = x_{vd}$ during negative slope phase. In fact, note that due to the capacitive load, oil flow is almost null and hence the valve plunger is on the upper or lower threshold displacement, thus leading to the hysteresis in the $p_u(i_e^*)$ characteristic. For current $i_e^* \geqslant 2.1$ A, pressure p_u is saturated at the supply pressure $p_s \cong 5$ MPa.

2.4.2. Reduced-order model

In this section, the frequency analysis of the gearbox actuator is developed, in order to enlighten the dependance of the pressure control loop bandwidth on the electro-magnetic, mechanical and hydraulic model, namely servovalve, pipeline and actuator parameters.

It is worth noting that the gearbox dynamics is nonlinear and hence, in principle, frequency analysis could be performed only on the system linearization in the neighborhood of an equilibrium point. Considering for simplicity the hydraulic actuator at constant volume, at the equilibrium (with constant command current) the valve plunger is in the dead-zone. On the other hand, since the nonlinear oil flow function $q_u(x_v, p_u)$ in (5) is not differentiable with respect to x_v in x_{vd} and x_{vf} and is characterized by null flow/displacement gain for $x_v \in (x_{vd}, x_{vf})$, it is not possible to define a linearized model for the servovalve subsystem (5).

However, linearization can be performed by exploiting the presence of a dither signal superimposed to the servovalve current. Dither is a high frequency signal which is added to nonlinear systems with the aim of averaging strong nonlinearities [16, Chapter 8,20]. Generally

speaking, dither frequency is higher than cut-off frequency, hence dither is filtered by the system and its "low-frequency" effect is to allow the approximation of the system behaviour with a smoother one. Application of dither is a well-known solution for mechanical and hydraulic systems with stick-slip friction or relay systems. One of the theoretical frameworks for stability analysis of systems with dither is the averaging method (see [21] for general theory and [22–24] for application to nonlinear systems with dither).

In the considered case, dither is exploited to smooth the nonlinearity coming from Bernoulli's equation (5) combined with the dead-zone of the overlapped servovalve. Based on the nonlinear model of the gearbox actuator and assuming a sinusoidal dither signal, time-scale separation can be enlightened and exploited to define a reduced-order model. In particular, three different time scales come out: (1) the fast dynamics of the sensing chamber pressure and pipeline resonances, (2) the dither excitation frequency, equal to 100 Hz, and (3) the slow electro-magnetic and mechanical model of the servovalve and the dominant hydraulic dynamics. Thanks to dither, the main feature of the reduced-order model is that it is an "averaged" version of the full-order one, characterized by a smooth position/user port oil flow function: in fact, the effect of dither is equivalent to superimpose a high-frequency sinusoidal signal to the valve displacement.

The reduced-order system is expressed by the 4th order model

$$
\begin{aligned}
\dot{x}_v &= v_v,\\
\dot{v}_v &= -\frac{k_v}{m_v}x_v - \frac{b_v}{m_v}v_v - \frac{A_c}{m_v}p_u + \frac{f_e}{m_v} + \frac{f_{v0}}{m_v},\\
\dot{f}_e &= -\frac{1}{\tau_e}f_e + \frac{k_f}{\tau_e}i_e^*,\\
\dot{p}_u &= \frac{1}{C_p}\frac{\pi}{2}q_{u,av}(x_v,p_u),\\
q_1 &= 0,\\
p_1 &= p_u + \frac{2\alpha_p^2}{\pi}\left(\frac{R_p\beta_p}{\alpha_p} - \frac{4Z_0D_n\pi}{\alpha_p^2}\right)q_{u,av}(x_v,p_u),\\
p_c &= p_u,
\end{aligned}
\tag{8}
$$

where the averaged oil flow $q_{u,av}(x_v,p_u)$ is derived from (5) as

$$
q_{u,av}(x_v,p_u) = \frac{1}{2\pi}\int_0^{2\pi} q_u(x_v + x_d\cos\tau, p_u)\mathrm{d}\tau,
$$

where x_d is the maximum amplitude of the valve plunger displacement induced by dither. Details on model derivation, based on successive applications of singular perturbation method and averaging theory [21,25], are reported in Appendix A.

As an example, in Fig. 8 the position vs oil flow characteristics $q_u(x_v,p_u)$ and its averaged version $q_{u,av}(x_v,p_u)$, for $p_u = 25\times10^5$ Pa and with $x_d = 6.4\times10^{-5}$ m as in the available experimental set-up, are shown.

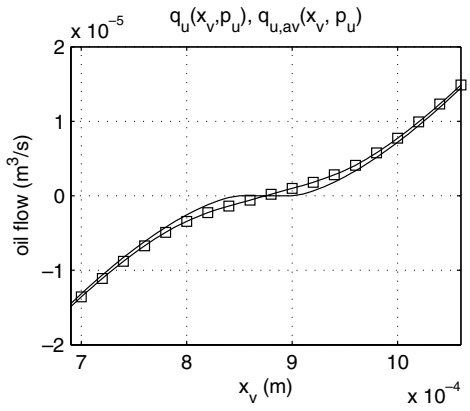

Fig. 8. Oil-flow characteristics $q_u\ (x_v,p_u)$ (solid) and its averaged version $q_{u,av}(x_v,p_u)$ (marked) for $p_u = 25\times10^5$ Pa.

Given a constant command current i_e^*, the equilibrium point of (8) is $(x_v, v_v, f_e, p_u)^{\mathrm{T}} = (x_{ve}, 0, k_f i_e^*, p_{ue})^{\mathrm{T}}$ with x_{ve}, p_{ue} such that $q_{u,av}(x_{ve},p_{ue}) = 0$ and $k_v x_{ve} + A_c p_{ue} = k_f i_e^* + f_{v0}$. Performing linearization of model (8) at a given equilibrium point, small signal frequency analysis of the hydraulic gearbox actuator model can be carried out. In Fig. 9 the Bode plots of $\frac{P_1(\omega)}{I_e^*(\omega)}$ for $p_{ue} = 10\times10^5$ Pa, 25×10^5 Pa, 40×10^5 Pa are shown. A meaningful insight of the system structure can be drawn from Fig. 6. The bandwidth of the pressure control loop, relating command current i_e^* to the delivered actuator pressure p_u, is determined by the cascade of: (a) the electro-magnetic valve subsystem, characterized by 1st order dynamics with 10 ms time constant, and (b) the valve mechanical and the main hydraulic pipeline dynamics, characterized by a bandwidth equal to 400 rad/s and poorly damped complex poles. It results that eigenvalue positions and the overall system bandwidth, which is approximatively 100 rad/s, do not depend significatively on the equilibrium point.

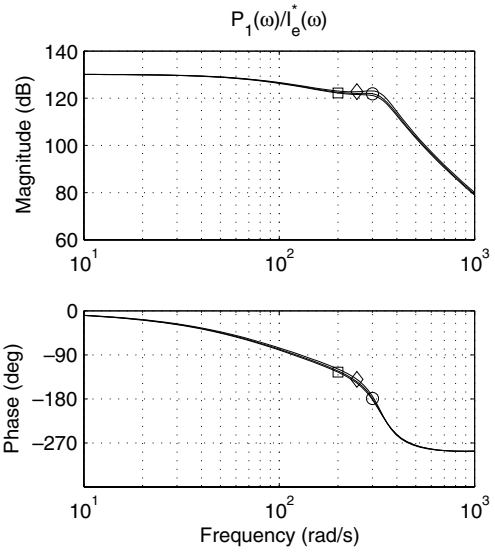

Fig. 9. Bode plot of the linearized model $P_1(\omega)/I_e^*(\omega)$ for $p_u = 10\times10^5$ Pa (□), $p_u = 25\times10^5$ Pa (◇), $p_u = 40\times10^5$ Pa (○).

3. Clutch actuator model

The automated clutch is constituted by a standard dry clutch controlled by an electro-hydraulic servo. As depicted in Fig. 10, the clutch actuator is constituted by disks between the flywheel and the clutch plate, whose surfaces are covered with high-friction materials. The electro-hydraulic clutch actuator, which is driven by a three-way spool servovalve [7,16], applies pressure to control the displacement of the clutch piston, which pushes on the release bearing. The transmitted torque T_c can be thought as stick-slip friction, while the maximum transmissible torque (related to static friction) is modulated by the normal force applied to clutch disks. In [7] a clutch actuator model focusing on the hydraulic part and involving the release bearing position as output variable has been developed. In this section, the model is refined considering the relation between the force applied to the release bearing and the transmitted clutch torque.

When no external force is applied, flywheel and clutch disks are pressed together by Belville and pre-load springs and hence engine torque can be transmitted. In order to release the clutch, the hydraulic piston pushes the release bearing: the Belville spring, acting as a lever, reduces the normal force applied to the clutch plates, thus separating friction disks. Note that the Belville spring acts both as a spring and a lever with variable coupling ratio; hence, the steady-state piston force is related to the force applied to the clutch plate by a nonlinear relation dependent on the clutch piston displacement. With these considerations in mind, the mechanical dynamics of the release bearing and the clutch plate is given by

$$\begin{aligned} m_{c1}\ddot{x}_{c1} &= -b_{c1}(\dot{x}_{c1}) - f_{c,b}(x_{c1}) + A_{c,p}p_{c,p}, \\ m_{c2}\ddot{x}_{c2} &= -b_{c2}(\dot{x}_{c2}) - c_r(x_{c1})f_{c,b}(x_{c1}) - k_c x_{c2} - f_{c0} + n_c, \\ 0 \leqslant x_{c2} &\perp n_c \geqslant 0, \end{aligned} \tag{9}$$

where $f_{c,p} = A_{c,p}p_{c,p}$ represents the force applied by the electro-hydraulic actuator to the piston and n_c is the unilateral constraint force between the two disks.

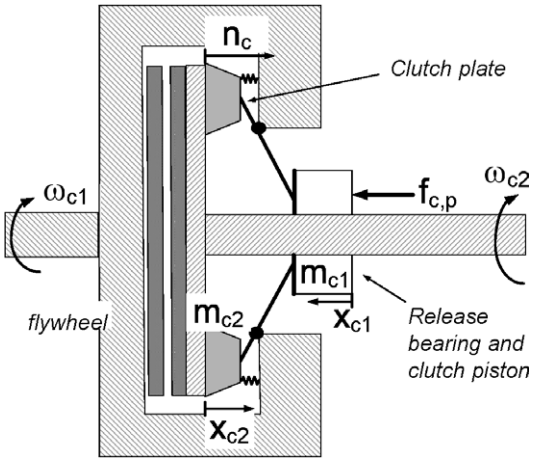

Fig. 10. Schematic diagram of the clutch actuator.

Remark 3.1. Note that when $f_{c,p} = 0$ the clutch is locked, i.e. $x_{c2} = 0$, thanks to the pre-load springs. From (9), it follows that with locked clutch the normal constraint force is given by $n_c = f_{c0} + c_r(x_{c1})f_{c,b}(x_{c1}) \geqslant 0$, while when the clutch disks are not in contact it holds $n_c = 0$. Therefore, neglecting inertial and friction terms in (9), the normal constraint force n_c is a nonlinear function of the clutch position x_{c1}, and hence of the pressure $p_{c,p}$ applied by the clutch actuator.

Assuming a stick-slip friction model [20], the maximum torque T_{cM} transmissible by the disks is dependent on the axial force n_c applied to the clutch plate through the so-called clutch transmissibility curve. Hence, it follows that it is possible to control the maximum transmissible torque T_{cM} by controlling the clutch piston position x_{c1}. According to the stick-slip friction model, the torque transmitted by the clutch is expressed by

$$T_c = \begin{cases} T_c^* & \text{if } (\omega_{c1} = \omega_{c2}) \text{ and} \\ & (|T_c^*| \leqslant T_{cM}(n_c))(\text{locked}), \\ T_{cM}(n_c)\cdot \operatorname{sign}(\omega_{c1} - \omega_{c2}) & \text{otherwise} \\ & (\text{slipping}), \end{cases} \tag{10}$$

where T_c^*, whose expression will be defined in Section 4, represents the transmitted torque maintaining locked clutch disks, i.e. $\omega_{c1} = \omega_{c2}$ and $\dot{\omega}_{c1} = \dot{\omega}_{c2}$. Note that in (10) "locked" refers to condition with $x_{c2} = 0$, $\omega_{c1} = \omega_{c2}$ and effective transmitted torque lower than the maximum one, while "slipping" refers or to condition with slipping disks or to detached disks, when $n_c = 0$ and hence $T_{cM} = 0$.

4. Model of transmission shafts

In order to analyze and validate the actuator models developed, it is necessary to combine them with the transmission shaft dynamics. For this purpose, a simplified linear model of the driveline mechanical dynamics is presented and integrated with the actuator models, hence obtaining an overall driveline model with hybrid structure. Even though the introduced hypothesis are restrictive and not realistic, they can be assumed for gear shift modelling purposes, since they do not have high influence on the model. Hence, despite the simplicity of the driveline model developed, it is possible to accurately describe the actuators behaviour and their effect on the driveline during the gear shift.

As shown in Fig. 1, the driveline can be thought as composed by engine, clutch, gearbox, wheels and vehicle inertia, connected by flexible damped transmission shafts. Each shaft (crankshaft, main and secondary shaft) is modelled as a spring-damper element connecting two equivalent inertias, relative to the shaft and the loads. Each shaft is characterized by its input/output speeds and spring torsional displacement. Relations between shaft speeds and transmitted torques depend on clutch and gearbox operating conditions.

The engine is modelled as an ideal torque actuator characterized by a constant inertia connected through the crankshaft to the flywheel and the clutch disks. Torque T_e represents the net torque generated by the engine, considering also friction losses. For gear shift control purposes, a detailed model of discontinuous torque generation in the internal combustion engine is not considered, hence high frequency torque components dependent on the crankshaft angle are not taken into account.

Elements between gearbox and wheels (secondary and axle shafts, differential drive and tires) can be modelled as a unique equivalent mass-spring-damper system under the following assumptions. The differential drive, which has a constant speed ratio, is considered to be rigidly connected to the gearbox. Backlash is neglected in the shaft dynamics. The viscous and elastic effects of secondary and axle shafts and tires are lumped into a unique equivalent spring-damper element. A simplified model of the tire/road interaction is considered, since infinite tire stiffness and no tire slipping are assumed, i.e. output axle speed is algebraically related to vehicle speed. Torque T_w, representing the equivalent load torque applied to the wheels due to road friction, aerodynamical drag and gravitational force acting on the vehicle, is assumed to be a slowly varying disturbance input.

According to previous considerations, the following mass-spring-damper dynamics, obtained from Newton's law, describe the transmission shafts (see also Fig. 1)

$$\begin{aligned} J_e\dot{\omega}_e &= T_e - T_{ec},\\ J_{c1}\dot{\omega}_{c1} &= T_{ec} - T_c,\\ J_{c2}\dot{\omega}_{c2} &= T_c - T_{cg},\\ J_{g1}\dot{\omega}_{g1} &= T_{cg} - b_g\omega_{g1} - T_{g1},\\ J_{g2}\dot{\omega}_{g2} &= T_{g2} - T_{gw},\\ J_w\dot{\omega}_w &= T_{gw} - T_w, \end{aligned} \tag{11}$$

with

$$\begin{aligned} T_{ec} &= k_{ec}\theta_{ec} + b_{ec}\omega_{ec},\\ \dot{\theta}_{ec} &= \omega_{ec} = \omega_e - \omega_{c1},\\ T_{cg} &= k_{cg}\theta_{cg} + b_{cg}\omega_{cg},\\ \dot{\theta}_{cg} &= \omega_{cg} = \omega_{c2} - \omega_{g1},\\ T_{gw} &= k_{gw}\theta_{gw} + b_{gw}\omega_{gw},\\ \dot{\theta}_{gw} &= \omega_{gw} = \omega_{g2} - \omega_w. \end{aligned} \tag{12}$$

Note that torques T_{ec}, T_{cg}, T_{gw} represent viscous and elastic torques transmitted through the transmission shafts. Torque T_c transmitted by the clutch and torques T_{g1}, T_{g2} transmitted by the gearbox are utilized to express the interconnections between shafts. Their dependency on actuator behaviour, i.e. locking/slipping of the clutch and configuration of the gearbox, has been defined in previous sections.

Remark 4.1. As an example, according to the finite state automaton in Fig. 4 and the hybrid clutch actuator model of Section 3, when the clutch is locked and a speed with gear ratio $r = r_i$ is engaged, shaft speeds are related by $\omega_{c1} = \omega_{c2} = \omega_c$ and $\omega_{g1} = r\omega_{g2} = \omega_g$, and values of torques $T_c = T_c^*$ and $T_{g1} = T_{g2}/r = T_g^*$ are such to guarantee that the shafts remain connected, i.e. $\dot{\omega}_{c1} = \dot{\omega}_{c2}$ (locked clutch) and $\dot{\omega}_{g1} = r\dot{\omega}_{g2}$ (engaged gear). In this case, clutch and gearbox dynamics in (11) reduce to

$$\begin{aligned} &(J_{c1} + J_{c2})\dot{\omega}_c = T_{ec} - T_{cg},\\ &\left(J_{g1} + \frac{J_{g2}}{r^2}\right)\dot{\omega}_{g1} = T_{cg} - b_g\omega_g - \frac{T_{gw}}{r} \end{aligned}$$

and torques transmitted by clutch and gearbox are obtained as

$$\begin{aligned} T_c^* &= \frac{J_{c1}J_{c2}}{J_{c1} + J_{c2}}\left(\frac{T_{ec}}{J_{c1}} + \frac{T_{cg}}{J_{c2}}\right),\\ T_g^* &= \frac{J_{g1}J_{g2}}{r^2J_{g1} + J_{g2}}\left(\frac{T_{cg} - b_g\omega_{g1}}{J_{g1}} + \frac{rT_{gw}}{J_{g2}}\right). \end{aligned}$$

Note that the equivalent secondary shaft and wheel inertias referred to the engine are given by $\frac{J_{g2}}{r^2}$ and $\frac{J_w}{r^2}$ respectively.

5. Model validation and experimental results

In this section, the model proposed is validated with respect to experimental data relative to both *ad hoc* tests and standard operations performed during gear shift. The analysis proceeds in this way. First, dynamical properties of the gearbox actuator are investigated by means of tests performed on a laboratory test-bench. Then, the overall model is analyzed and validated on various gear shift transients. The proposed model has been realized in Matlab/Simulink/Stateflow.

Parameters of the clutch and gearbox actuator models have been identified from data sheets on the basis of theoretical and physical laws, apart spring pre-load values, which have been determined through experiments. Differently, viscous and elastic parameters of the drive-train model and force/torque gains k_{gD}, k_{gS} have been determined by means of experimental tests. In this case, numerical estimation methods based on nonlinear least square optimization [26] have been utilized for parameter identification, comparing measured and simulated signals. It is worth noting that it is not possible to identify these parameters from design data, since the drive-train is described by a reduced-order model. Parameter values are reported in Tables B.1–B.5, where "T" and "E" stand for theoretically-based parameter identification procedures or experimentally-based numerical estimation methods.

5.1. Gearbox actuator

As shown in Fig. 11, the laboratory test-bench utilized for the gearbox model validation is equipped with a gearbox actuator, which is sensorized and interfaced with a rapid prototyping station, composed by a dSpace AutoBox platform connected to a host PC. The dSpace boards

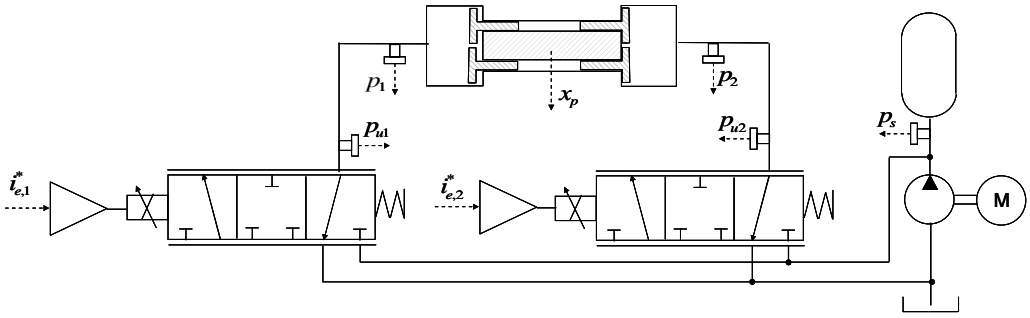

Fig. 11. Experimental test-bench.

allows for actuator control (servovalve coils are actuated through two switching amplifiers) and for data acquisition (measured pressures are output servovalve pressures p_{u1}, p_{u2}, actuator pressures p_1, p_2 and supply pressures p_s, while the piston position x_p is acquired by a potentiometer). All data are sampled every 5 ms with 10 bit A/D converters. The testing software on the PC provides a virtual oscilloscope for data monitoring and acquisition and an interface with the Simulink environment. The supply pressure is maintained almost constant thanks to a high pressure accumulator filled by a pump.

For validation of the gearbox model, experiments are performed in order to analyze pipeline dynamics and tappets and piston motion. To this purpose, during tests the fork is not connected to the gearbox and is free to move. Step-wise valve currents have been applied, starting from different initial piston displacements (engaged even or odd gear, neutral phase).

Aiming to validate the model with locked mechanical actuator, in the first test (see Fig. 12) 1.7 A step-wise $i^*_{e,2}$ command current is applied at $t = 50$ ms with the piston in the left position (refer to Fig. 3), while keeping $i^*_{e,1} = 0$ A. Piston and tappets position remain constant, while from transient profiles of p_{u2}, p_2 a 10 ms pipeline time delay and negligible resistive losses, due to almost null oil-flow, are enlightened.

In the second test, reported in Fig. 13, the same 1.7 A step-wise command current profile $i^*_{e,2}$ is applied with the piston in the right position, with $i^*_{e,1} = 0$ A. In this case, piston and tappets move toward the left mechanical stops, reaching it in 80 ms. During transient, pressures p_{u2} and p_2 have non null regulation error with respect to the steady-state pressure vs current characteristic in Fig. 7. This is due to non-null oil flow determined by the increase of the chamber volume, which can be roughly approximated by $A_2 v_p$ during the phase with joined tappet and piston, and by $A_{2,i} v_p$ during the last phase, with the tappet against the internal stop ($x_2 = 0$). The oil flow required to move the piston can be considered as a disturbance q_{1d} acting on the closed-loop pressure dynamics, as depicted also in Fig. 6. Moreover, comparison of p_{u2} and p_2 profiles enlightens pressure loss in the pipe, which can be expressed by the steady-state characteristic of the pipeline as $8 Z_0 D_n q_{1d}$.

5.2. Overall model

The overall driveline model has been validated with respect to experimental data relative to gear shifts

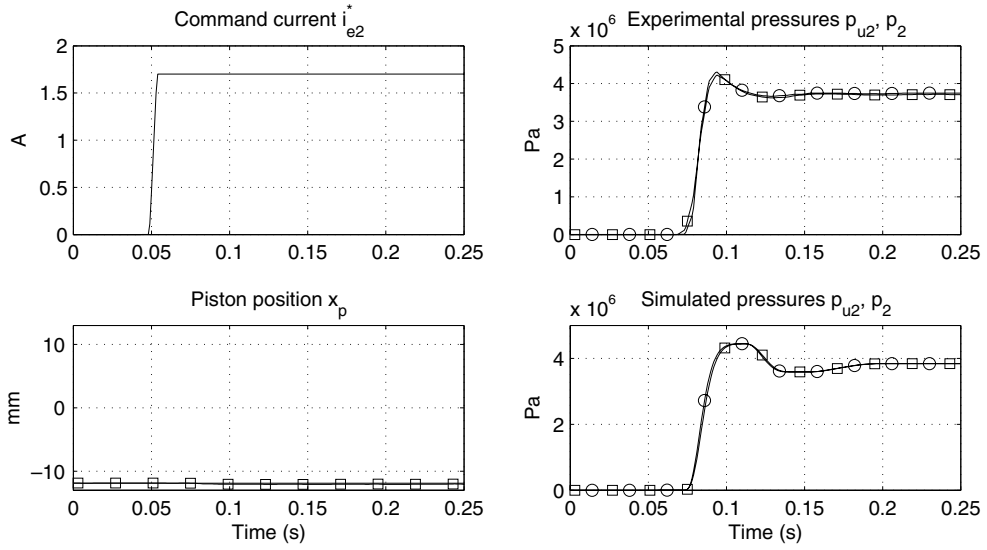

Fig. 12. Dynamic response with 1.7 A step-wise current $i^*_{e,2}$ with initial piston position $x_p = -12.2$ mm. In the bottom left graph: experimental x_p (marked), simulated x_p (solid). In the right graphs: pressure p_{u2} (□), p_2 (○).

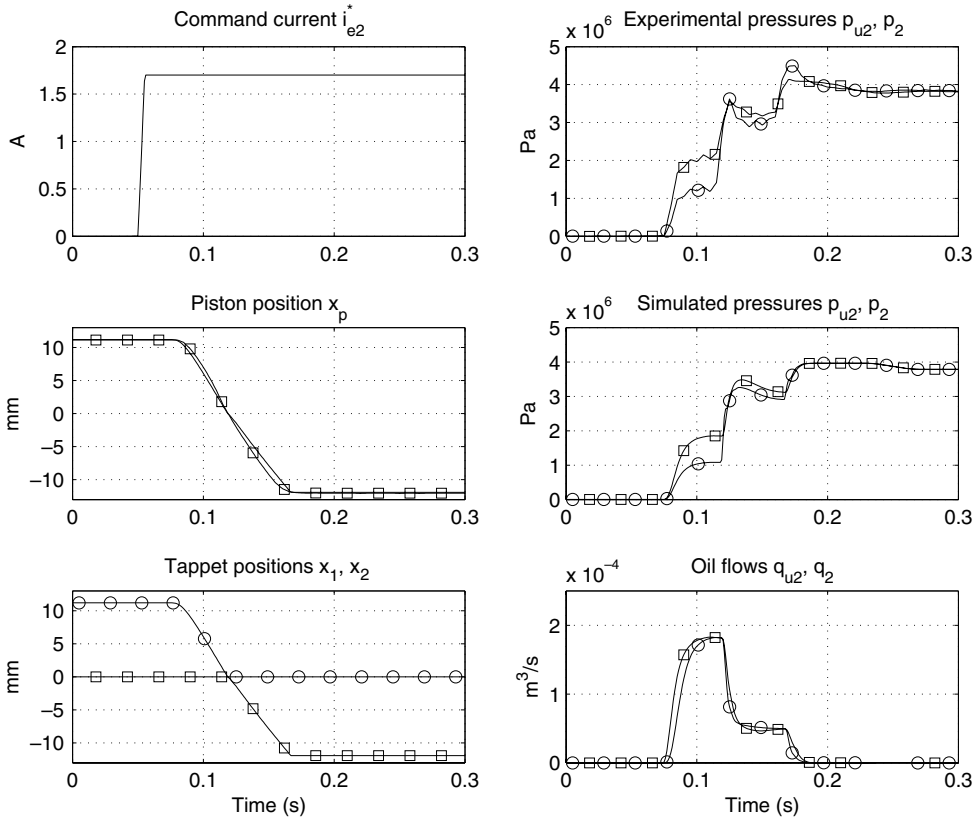

Fig. 13. Dynamic response with 1.7 A step-wise current $i^*_{e,2}$ with initial piston position $x_p = 12.2$ mm. Left graphs: experimental x_p (marked) and simulated x_p (solid); simulated tappet positions x_1 (□), x_2 (○). Right graphs: pressure p_{u2} (□) and p_2 (○); oil flow q_{u2} (□) and q_2 (○).

performed with a commercial sport car with a $V8$ 4250 cc engine with 450 Nm maximum torque and 290 kW power. The Electronic Control Unit (ECU) devoted to gear shift management has been interfaced with a dSpace AutoBox for monitoring and data acquisition purposes. The following variables are utilized for parameter identification and model validation: measured engine speed ω_e, gearbox input shaft speed ω_{g1}, wheel speed ω_w, applied clutch pressure $p_{c,p}$ and clutch position x_{c1}, gearbox piston position x_p and gearbox valve command currents $i^*_{e,1}, i^*_{e,2}$. Engine torque T_e is the estimated torque obtained by the ECU, taking into account friction losses. Load wheel torque T_w is estimated from experimental data and it is approximated with a constant value during experiments. The maximum transmissible clutch torque curve T_{cM} is estimated from the nominal transmissibility curve, Belville spring force and clutch position. Note that many parameters, e.g. $T_{cM}(n_c)$, $c_r(x_{c1})$, $f_{c,b}(x_{c1})$ for clutch subsystem, are time-varying and depend on aging and temperature. Since the focus of the paper is not on parameter estimation methods, all the parameters are assumed to be estimated under the same operating conditions of the tests.

In Fig. 14 experimental and simulation results relative to the gear shift from 1st to 2nd speed are compared. In the simulation, control inputs, i.e. engine torque, gearbox valve currents and clutch pressure shown in graphs (a), (e), (i) have been imposed to the model. Real and simulated engine and shaft speeds are compared in graphs (b) and (d) respectively, while transmitted torques are shown in graph (c). In graphs (f), (h) simulated gearbox pressures p_1, p_2 are shown, and experimental and simulated piston displacements are compared in graph (g). With respect to previous analysis on the gearbox actuator, in this case also reaction forces of gearbox cogwheels and devices such as the synchronizer, act as disturbances on the piston. In graph (j), experimental and simulated clutch piston displacement x_{c1} are comparatively reported, from which it follows that an accurate model of the clutch actuator, influencing the driveline behaviour through the transmissibility curve, is obtained.

The gear shift starts with 4000 rpm engine speed and constant 200 Nm engine torque, with 20 Nm load wheel torque, locked clutch and engaged 1st gear. At the gear shift request at $t = 10$ ms, engine torque goes to -90 Nm, clutch is required to open applying pressure $p_{c,p}$ to the clutch plate and gearbox current $i^*_{e,1}$ is applied in order to move the gearbox piston and to disengage current speed (see profile of pressure p_1). Engine and main shaft speeds decrease and, when the gearbox transmitted torque is lower than the disengaging threshold, the 1st gear disengages; at $t = 0.11$ s piston moves from the disengaging phase ($x_p \cong -5$ mm) to the neutral one. At the same time, clutch opens and, since the maximum clutch transmissible torque decreases, it starts slipping at $t = 0.155$ s (note that due to shaft stiffness it holds $\omega_e \cong \omega_{c1}$ and $\omega_{c2} \cong \omega_{g1}$). The gearbox is neutral from 0.11 s to 0.15 s, then it switches to synchronization phase, with constant piston position

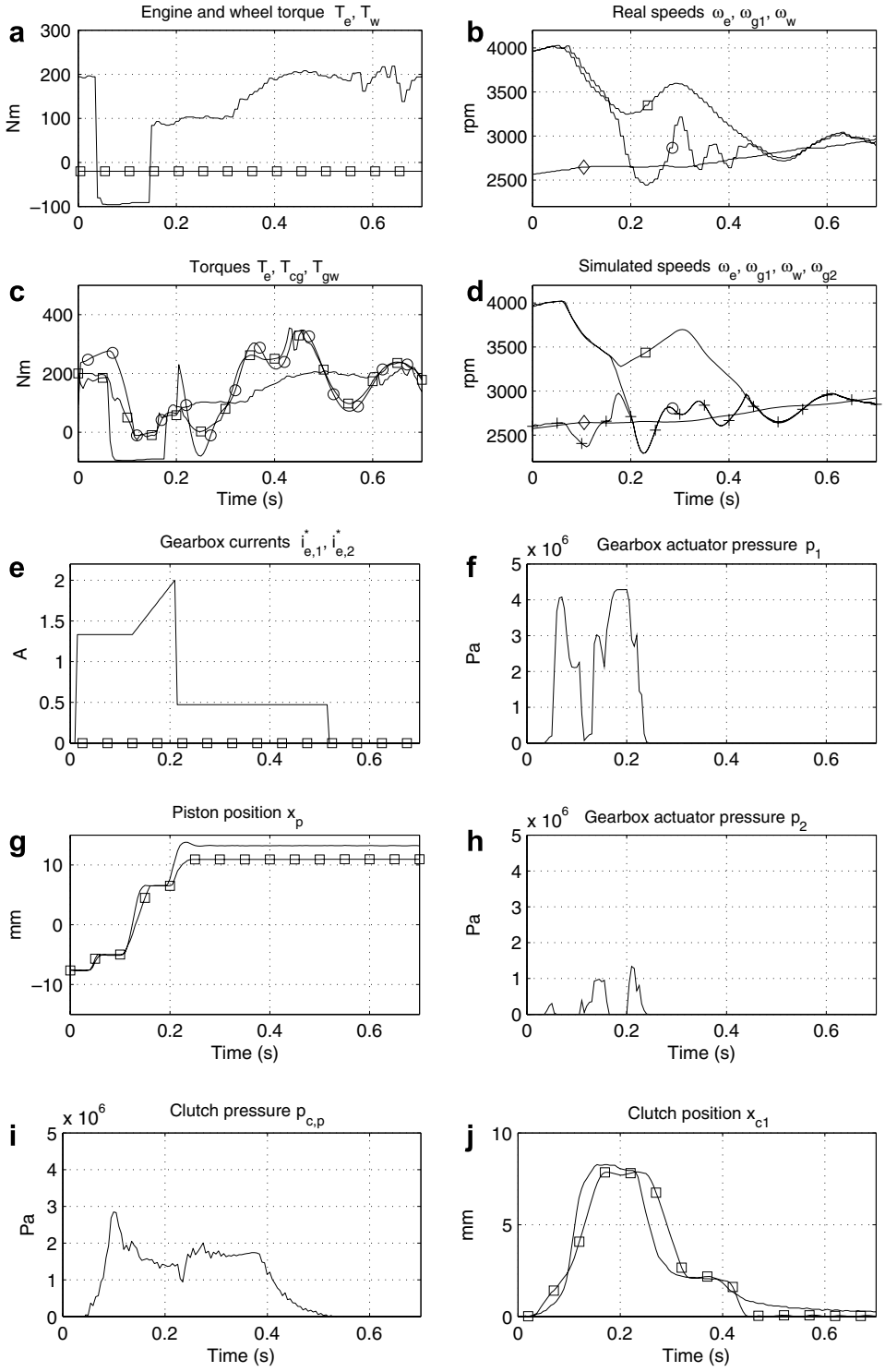

Fig. 14. First to second gear shift transient with 4000 rpm initial engine speed. (a) Engine torque T_e (solid) and wheel torque disturbance T_w (marked), (b), (d) real and simulated speeds ω_e (□), ω_{g1} (○), $r_2 \times \omega_w$ (◇) and simulated $r_2 \times \omega_{g2}$ (+), (c) engine torque T_e and simulated torques T_{cg} (□), T_{gw}/r_2 (○), (e) gearbox currents $i^*_{e,1}$ (solid), $i^*_{e,2}$ (marked), (f), (h) simulated gearbox actuator pressures p_1, p_2, (g) gearbox piston position x_p: experimental (solid), simulated (marked), (i) clutch actuator pressure $p_{c,p}$, (j) clutch piston position x_{c1}: experimental (solid), simulated (marked).

$x_p \cong 6.5$ mm. From 0.15 s, pressure is applied to the synchronizer, in order to engage the 2nd speed with ratio r_2 between ω_{g1} and ω_{g2}. At 0.21 s it holds $\omega_{g1} = r_2\omega_{g2}$, hence the 2nd speed is engaged and the gearbox piston moves toward the stop at 0.24 s. Meanwhile, engine torque is increased up to the initial value and the clutch starts closing: from 0.3 s to 0.45 s the clutch slips until crankshaft output speed and main shaft input speed are equal. After the clutch locks ($\omega_{c1} = \omega_{c2}$), damped oscillations are present in the driveline shaft speeds and transmitted torques.

In Fig. 15 experimental and simulation results relative to a 2nd to 1st gear shift are presented. When the gear shift is required at 50 ms, engine speed is 2700 rpm and −90 Nm engine torque is applied. Clutch is requested to open applying pressure $p_{c,p}$ to the release bearing. Note that with respect to previous tests, better agreement between simulated and experimental clutch position x_{c1} is obtained, since the hydraulic clutch actuator dynamics are less excited due to slower transients. Second speed disengagement, performed applying pressures to the piston, occurs at 0.3 s, when the gearbox torque is almost null. After the neutral phase, lasting from 0.3 s to 0.63 s, the piston moves to

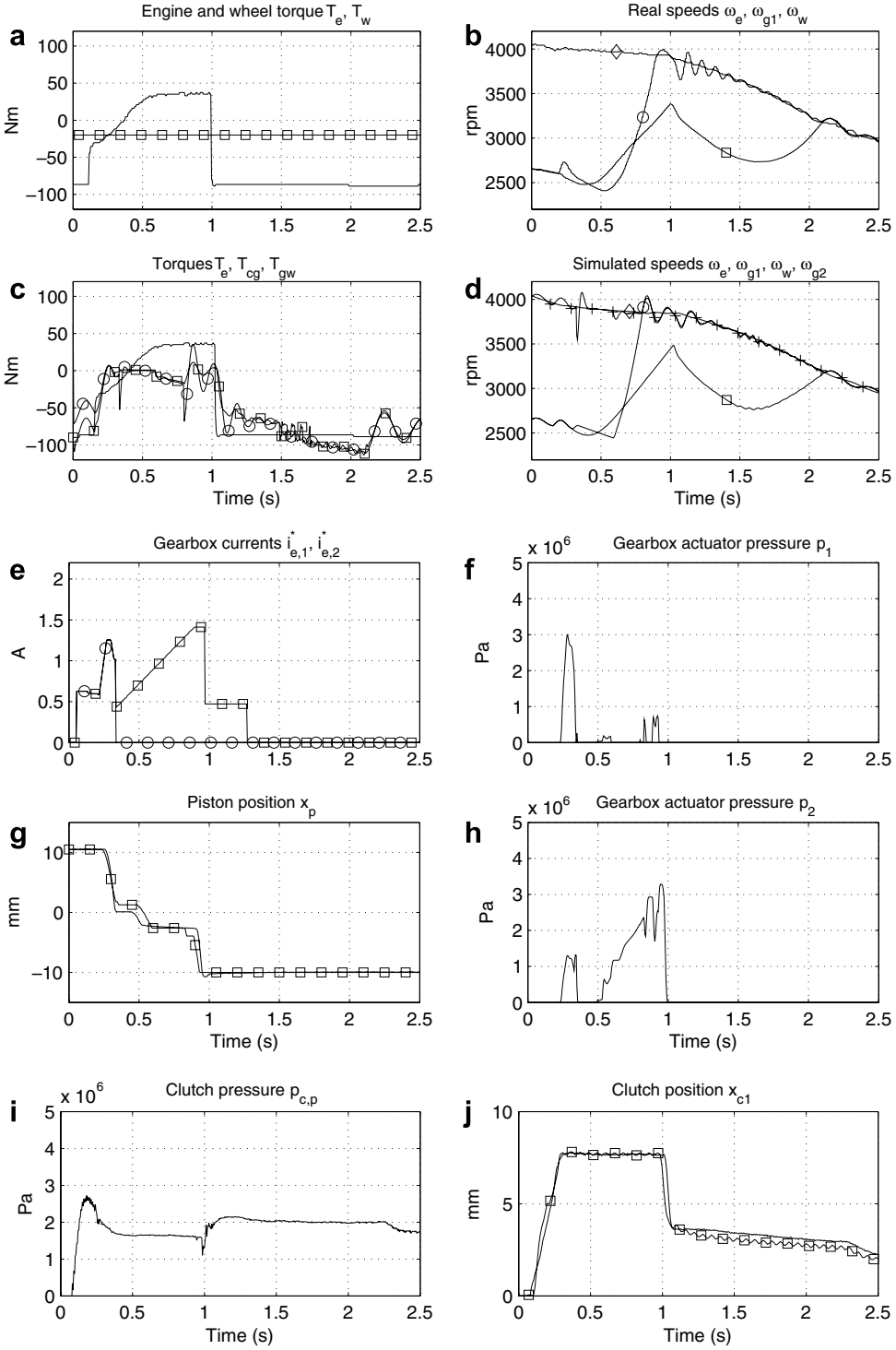

Fig. 15. Second to first gear shift transient. (a) Engine torque T_e (solid) and wheel torque disturbance T_w (marked), (b), (d) real and simulated speeds ω_e (□), ω_{g1} (○), $r_1 \times \omega_w$ (◇) and simulated $r_1 \times \omega_{g2}$ (+), (c) engine torque T_e and simulated torques T_{cg} (□), T_{gw}/r_1 (○), (e) gearbox currents $i^*_{e,1}$ (○), $i^*_{e,2}$ (□), (f), (h) simulated gearbox actuator pressures p_1, p_2, (g) gearbox piston position x_p: experimental (solid), simulated (marked), (i) clutch actuator pressure $p_{c,p}$, (j) clutch piston position x_{c1}: experimental (solid), simulated (marked).

the synchronization threshold −2.5 mm, pressure p_2 is applied to the synchronizer and main shaft speed ω_{g1} increases. When $\omega_{g1} = r_1 \times \omega_{g2}$, the 1st gear engages and the piston moves to the mechanical stop. Meanwhile, from 0.1 s to 1.0 s the engine speed is increased by applying engine torque, in order to reduce duration of the clutch slipping phase. At 1.0 s clutch starts closing and engine torque goes to −90 Nm. The clutch slipping phase ends when $\omega_e \cong \omega_{c1} = \omega_{c2} \cong \omega_{g1}$ at 2.1 s.

Comparison of simulated and experimental profiles during gear shift shows good matching between the proposed model and the real system. Hence, the proposed model is able to capture the gearbox and clutch actuators behaviour and to enlighten the interaction between actuators and the main drivetrain dynamics.

6. Conclusions

Detailed physically-based models of electro-hydraulic servo-actuated gearbox and clutch of a car equipped with an AMT have been developed and integrated with a simplified model of transmission shafts and engine. As enlightened by the comparison of experimental and simulated results, the presented model shows the influence of the actuators for gear shift control on the gear shift quality and performance, which represents a relevant aspect for system and control algorithm design. The gearbox actuator model, whose parameters have been determined by a physically-based identification procedure, is able to reproduce in an accurate way the gearbox dynamics during gear shifts.

Appendix A. Reduced-order model of the gearbox actuator

A simplified model of the gearbox actuator obtained from (1) and (3)–(6) is recalled here for the sake of clarity:

$$
\begin{aligned}
\dot{x}_v &= v_v,\\
\dot{v}_v &= -\frac{k_v}{m_v}x_v - \frac{b_v}{m_v}v_v - \frac{A_c}{m_v}p_c + \frac{f_{v0}}{m_v} + \frac{f_e}{m_v},\\
\dot{f}_e &= -\frac{1}{\tau_e}f_e + \frac{1}{\tau_e}k_f\left(i_e^* + i_{e,d}\right),\\
\dot{p}_u &= \frac{1}{C_p}\left(-\frac{\pi}{2}q_1 + \frac{\pi}{2}q_u(x_v, p_u)\right),\\
\dot{q}_1 &= \frac{1}{L_p}\left(\frac{\pi}{2}\frac{1}{\alpha_p^2}p_u - \frac{R_p\beta_p}{\alpha_p}q_1 - \frac{\pi}{2}\frac{1}{\alpha_p^2}p_1 + R_p' q_u(x_v, p_u)\right),\\
\dot{p}_1 &= \frac{1}{C_1}q_1,\\
\dot{p}_c &= \frac{1}{\tau_c}(p_u - p_c).
\end{aligned}
\tag{A.1}
$$

It is derived under the following simplifications and assumptions. In (3) Bernoulli forces are neglected, linear friction force $b_v v_v$ is supposed, a sinusoidal dither signal $i_{e,d}$ at frequency ω_d is superimposed to the command current i_e^* and q_u is defined by (5). In (4) terms dependent on volume variation and speed can be neglected, while in (1) the actuator volume is supposed to be constant (fixed x_p, x_1, x_2). Parameters are defined as $\tau_c = \frac{V_{c0}}{\beta g_c}$, $C_1 = \frac{V_{10}}{\beta}$ and $R_p' = \left(\frac{R_p\beta_p}{\alpha_p} - \frac{4Z_0\, D_n\pi}{\alpha_p^2}\right)$. Amplitude and phase of the sinusoidal dither signal at frequency ω_d can be expressed as functions of the induced valve plunger displacement, by inverting the electromechanical servovalve model and recalling (7). With the purpose of enlightening that the steady-state effect of dither is to add a sinusoidal component $\bar{x}_v$ on the plunger position, introduce the following preliminary definitions: $\bar{x}_v = x_d\cos\omega_d t$, $\bar{v}_v = -\omega_d x_d \sin\omega_d t$, $\bar{f}_e = -(m_v\omega_d^2 - k_v)x_d\cos\omega_d t - b_v\omega_d x_d \sin\omega_d t$, $i_{e,d} = \frac{1}{k_f}(\tau_e\dot{\bar{f}}_e + \bar{f}_e)$. In the following, (A.1) is rewritten in standard form in order to apply singular perturbation and averaging methods. In order to enlighten time-scale separation through comparison of the magnitude of model coefficients, it is necessary to apply scaling to the state and input variables. To this aim, first introduce error variables with respect to the dither-dependent evolution: $\tilde{x}_v = x_v - \bar{x}_v - \frac{f_{v0}}{k_v}$, $\tilde{v}_v = v_v - \bar{v}_v$, $\tilde{f}_e = f_e - \bar{f}_e$. Define scaled variables as $\tilde{x}_{vn} = \lambda_x\tilde{x}_v$, $\tilde{v}_{vn} = \lambda_v\tilde{v}_v$, $\tilde{f}_{en} = \lambda_f\tilde{f}_e$, $p_{un} = \lambda_p p_u$, $q_{1n} = \lambda_q q_1$, $p_{1n} = \lambda_p p_1$, $p_{cn} = \lambda_p p_c$, $q_{un} = \lambda_q\, q_u$, $i_{en}^* = \lambda_i i_e^*$. Scaling factors, defined by simulation analysis and based on physical considerations, are specified such that the magnitude of the scaled variables is $O(1)$ as $\lambda_x = 3\times10^2$, $\lambda_v = 1$, $\lambda_p = 10^{-6}$, $\lambda_q = 10^4$, $\lambda_f = 1$, $\lambda_i = 10^1$. Hence, system (A.1) is rewritten as

$$
\begin{aligned}
\dot{\tilde{x}}_{vn} &= a_n\tilde{v}_{vn},\\
\dot{\tilde{v}}_{vn} &= -\frac{k_{vn}}{m_{vn}}\tilde{x}_{vn} - \frac{b_{vn}}{m_{vn}}\tilde{v}_{vn} + \frac{1}{m_{vn}}\tilde{f}_{en} - \frac{A_{cn}}{m_{vn}}p_{cn},\\
\dot{\tilde{f}}_{en} &= -\frac{1}{\tau_e}\tilde{f}_{en} + \frac{k_{fn}}{\tau_e}i_{en}^*,\\
\dot{p}_{un} &= \frac{1}{C_{pn}}\left(-\frac{\pi}{2}q_{1n} + \frac{\pi}{2}q_{un}(\tilde{x}_{vn} + x_{dn}\cos\omega_d t, p_{un})\right),\\
\dot{q}_{1n} &= \frac{1}{L_{pn}}\left(\frac{\pi}{2}\frac{1}{\alpha_p^2}p_{un} - \frac{R_{pn}\beta_p}{\alpha_p}q_{1n} - \frac{\pi}{2}\frac{1}{\alpha_p^2}p_{1n}\right.\\
&\qquad \left. + R_{pn}' q_{un}(\tilde{x}_{vn} + x_{dn}\cos\omega_d t, p_{un})\right),\\
\dot{p}_{1n} &= \frac{1}{C_{1n}}q_{1n},\\
\dot{p}_{cn} &= \frac{1}{\tau_c}p_{un} - \frac{1}{\tau_c}p_{cn},
\end{aligned}
\tag{A.2}
$$

where $x_{dn} = \lambda_x x_d$ and $q_{un}(\tilde{x}_{vn} + x_{dn}\cos\omega_d t, p_{un}) = \lambda_q q_u(f_{v0}/k_v + \lambda_x^{-1}(\tilde{x}_{vn} + x_{dn}\cos\omega_d t), \lambda_p^{-1}p_{un})$ and normalized coefficients (labelled with "n") and other parameters directly follow from (A.1) and definition of scaled variables. Main feature of (A.2) is that, differently from (A.1), the effect of dither enters directly in the nonlinear function q_u through the sinusoidal displacement $\bar{x}_v$. This fact is profitable for application of averaging theory.

In the considered set-up, the dither signal is a 100 Hz square wave with 0.5 A peak-peak amplitude.

Approximating dither with its first harmonic, it follows that $x_d = 6.4 \times 10^{-5}$ m, i.e. comparable with the dead-zone of the overlapped valve (see Table B.1). Considering values in Tables B.1–B.3 and analyzing coefficients of (A.2), two-time scale is enlightened. In fact, partitioning state variables into slow $\mathbf{x}_s = (\tilde{x}_{vn}, \tilde{v}_{vn}, \tilde{f}_{en}, p_{un})$ and fast $\mathbf{x}_f = (q_{1n}, p_{1n}, p_{cn})$ components, system (A.2) can be expressed in compact form as

$$\begin{aligned} \frac{\mathrm{d}\mathbf{x}_s}{\mathrm{d}t} &= f_s(\mathbf{x}_s, t) + B_s \mathbf{x}_f + B_{us} i^*_{en}, \\ \frac{\mathrm{d}\mathbf{x}_f}{\mathrm{d}t} &= A_f \mathbf{x}_f + f_f(\mathbf{x}_s, t), \end{aligned} \tag{A.3}$$

where time-varying terms are due to dither-dependent plunger displacement $\bar{x}_v$. Defining bounding coefficients μ_s, μ_f for the dynamics (A.3) such that $|f_s(\mathbf{x}_s, t)| \leqslant \mu_s |\mathbf{x}_s|$, $\forall \mathbf{x}_s, t$, $|B_s| \leqslant \mu_s$, $|B_{us}| \leqslant \mu_s$ and $|f_f(\mathbf{x}_s, t)| \leqslant \mu_f |\mathbf{x}_s|$, $\forall \mathbf{x}_s, t$, $|A_f| \leqslant \mu_f$, it holds $\mu_s \sim 10^2 < \omega_d \sim 6 \times 10^2 < \mu_f \sim 10^4$, which corresponds to time-scale separation between the *slow* dynamics of the electro-magnetic and mechanical servo-valve system with the fundamental hydraulic line dynamics and the *fast* dynamics of the sensing chamber and pipeline resonances.

Now, derivation of the averaged model can be performed, following two steps: first, singular perturbation technique is applied to remove the fast state variables $\mathbf{x}_f$, then averaging method is applied in order to define the reduced-order model, with a smoothed version of the position/flow nonlinear characteristic.

In order to express the model (A.3) in the standard form for singular perturbation, define $\tau \triangleq \omega_d t$ and $\epsilon_f \triangleq \frac{\omega_d}{\mu_f}$, hence obtaining

$$\begin{aligned} \frac{\mathrm{d}\mathbf{x}_s}{\mathrm{d}\tau} &= \frac{1}{\omega_d} f_s(\mathbf{x}_s, \tau) + \frac{1}{\omega_d} B_s \mathbf{x}_f + \frac{1}{\omega_d} B_{us} i^*_{en}, \\ \epsilon_f \frac{\mathrm{d}\mathbf{x}_f}{\mathrm{d}\tau} &= \frac{1}{\mu_f} A_f \mathbf{x}_f + \frac{1}{\mu_f} f_f(\mathbf{x}_s, \tau), \end{aligned} \tag{A.4}$$

where from scaling and relations between μ_s, ω_d, μ_f, it follows that the right-hand side terms have $O(1)$ magnitude, and ϵ_f is a small coefficient (this property is related to the fact that hydraulic resonances and sensing chamber dynamics are faster than dither frequency).

System (A.4) is in standard form for singular perturbation, with slow variables $\mathbf{x}_s$ and fast variables $\mathbf{x}_f$ in the slow time τ. Performing singular perturbation reduction, the slow manifold is obtained by imposing $\epsilon_f = 0$ in the last equation of (A.4) as $\bar{\mathbf{x}}_f(\mathbf{x}_s, \tau) = -A_f^{-1} f_f(\mathbf{x}_s, \tau)$ (see also (A.2)), i.e.

$$\begin{aligned} q_{1n} &= 0, \\ p_{1n} &= p_{un} + \frac{2\alpha_p^2}{\pi} R'_{pn} q_{un}, \\ p_{cn} &= p_{un}. \end{aligned} \tag{A.5}$$

The boundary layer dynamics expressed with variables $\tilde{\mathbf{x}}_f = \mathbf{x}_f + A_f^{-1} f_f(\mathbf{x}_s, \tau) = (\tilde{q}_{1n}, \tilde{p}_{1n}, \tilde{p}_{cn})^{\mathrm{T}}$ in the fast time-scale $t_f \triangleq \frac{\tau}{\epsilon_f}$ is given by $\frac{\mathrm{d}\tilde{\mathbf{x}}_f}{\mathrm{d}t_f} = \frac{A_f}{\mu_f} \tilde{\mathbf{x}}_f$, i.e.

$$\begin{aligned} \frac{\mathrm{d}\tilde{q}_{1n}}{\mathrm{d}t_f} &= \frac{1}{\mu_f L_{pn}} \left(-\frac{\pi}{2} \frac{1}{\alpha_p^2} \tilde{p}_{1n} - \frac{R_{pn} \beta_p}{\alpha_p} \tilde{q}_{1n} \right), \\ \frac{\mathrm{d}\tilde{p}_{1n}}{\mathrm{d}t_f} &= \frac{1}{\mu_f C_{1n}} \tilde{q}_{1n}, \\ \frac{\mathrm{d}\tilde{p}_{cn}}{\mathrm{d}t_f} &= -\frac{1}{\mu_f \tau_c} \tilde{p}_{cn}, \end{aligned} \tag{A.6}$$

which is linear and exponentially stable, while the reduced-order model is obtained as

$$\frac{\mathrm{d}\mathbf{x}_s}{\mathrm{d}\tau} = \frac{1}{\omega_d} f_s(\mathbf{x}_s, \tau) - \frac{B_s}{\omega_d} A_f^{-1} f_f(\mathbf{x}_s, \tau) + \frac{B_{us}}{\omega_d} i^*_{en}, \tag{A.7}$$

i.e.

$$\begin{aligned} \frac{\mathrm{d}\tilde{x}_{vn}}{\mathrm{d}\tau} &= \frac{a_n}{\omega_d} \tilde{v}_{vn}, \\ \frac{\mathrm{d}\tilde{v}_{vn}}{\mathrm{d}\tau} &= -\frac{k_{vn}}{\omega_d m_{vn}} \tilde{x}_{vn} - \frac{b_{vn}}{\omega_d m_{vn}} \tilde{v}_{vn} + \frac{1}{\omega_d m_{vn}} \tilde{f}_{en} - \frac{A_{cn}}{\omega_d m_{vn}} p_{un}, \\ \frac{\mathrm{d}\tilde{f}_{en}}{\mathrm{d}\tau} &= -\frac{1}{\omega_d \tau_e} \tilde{f}_{en} + \frac{k_{fn}}{\omega_d \tau_e} i^*_{en}, \\ \frac{\mathrm{d}p_{un}}{\mathrm{d}\tau} &= \frac{1}{\omega_d C_{pn}} \frac{\pi}{2} q_{un}(\tilde{x}_{vn} + x_{dn} \cos\tau, p_{un}). \end{aligned} \tag{A.8}$$

Noting that $\mu_s < \omega_d$ and defining the small parameter $\epsilon_s \triangleq \frac{\mu_s}{\omega_d}$, the reduced-order model (A.7) can be rewritten as

$$\frac{\mathrm{d}\mathbf{x}_s}{\mathrm{d}\tau} = \epsilon_s \left[\frac{1}{\mu_s} f_s(\mathbf{x}_s, \tau) - \frac{B_s}{\mu_s} A_f^{-1} f_f(\mathbf{x}_s, \tau) + \frac{B_{us}}{\mu_s} i^*_{en} \right], \tag{A.9}$$

where dependency on τ is present through Bernoulli's equation only, functions f_s, f_f are 2π-periodic in τ, i.e. $f_s(\mathbf{x}_s, \tau) = f_s(\mathbf{x}_s, \tau + 2\pi)$, $f_f(\mathbf{x}_s, \tau) = f_f(\mathbf{x}_s, \tau + 2\pi)$, and from definition of μ_s all the coefficients in brackets are of order $O(1)$. Hence, the averaging method can be applied to (A.9). Defining the averaged flow, dependent on dither displacement amplitude x_d, as

$$q_{un,av}(\tilde{x}_{vn}, p_{un}) = \frac{1}{2\pi} \int_0^{2\pi} q_{un}(\tilde{x}_{vn} + x_{dn} \cos\tau, p_{un}) \mathrm{d}\tau, \tag{A.10}$$

it follows that the averaged model is

$$\begin{aligned} \frac{\mathrm{d}\tilde{x}_{vn}}{\mathrm{d}\tau} &= \frac{a_n}{\omega_d} \tilde{v}_{vn}, \\ \frac{\mathrm{d}\tilde{v}_{vn}}{\mathrm{d}\tau} &= -\frac{k_{vn}}{\omega_d m_{vn}} \tilde{x}_{vn} - \frac{b_{vn}}{\omega_d m_{vn}} \tilde{v}_{vn} + \frac{1}{\omega_d m_{vn}} \tilde{f}_{en} - \frac{A_{cn}}{\omega_d m_{vn}} p_{un}, \\ \frac{\mathrm{d}\tilde{f}_{en}}{\mathrm{d}\tau} &= -\frac{1}{\omega_d \tau_e} \tilde{f}_{en} + \frac{k_{fn}}{\omega_d \tau_e} i^*_{en}, \\ \frac{\mathrm{d}p_{un}}{\mathrm{d}\tau} &= \frac{1}{\omega_d C_{pn}} \frac{\pi}{2} q_{un,av}(\tilde{x}_{vn}, p_{un}). \end{aligned} \tag{A.11}$$

Note that (A.11) together with (A.5) are equivalent to (8) expressed in the physical variables and time. Since, for given command current $i^*_{en}(\tau)$, the origin of the error model of (A.11) with respect to the nominal solution is exponentially stable, from averaging theorem [21, Theorem 8.3] it follows that for sufficiently small difference in the initial conditions the solution $\mathbf{x}_{sa}(\tau)$ of (A.11) approximates the solution $\mathbf{x}_{sr}(\tau)$ of (A.8) with an error $O(\epsilon_s)$, i.e. $\mathbf{x}_{sa}(\tau) - \mathbf{x}_{sr}(\tau) = O(\epsilon_s)$. Since (A.8) is the reduced-order model of the singularly perturbed system (A.4) with exponentially stable boundary layer model (A.6), from Tikhonov's theorem on the infinite time interval [21, Theorem 9.4] it follows that the solution $\mathbf{x}_{sr}(\tau)$ and the quasi-steady state solution $\bar{\mathbf{x}}_f(\mathbf{x}_{sr}, \tau)$ defined in (A.5) asymptotically approximate the solution $\mathbf{x}_s(\tau)$, $\mathbf{x}_f(\tau)$ of the full-order model (A.2) with an error $O(\epsilon_f)$, i.e. $\mathbf{x}_{sr}(\tau) - \mathbf{x}_s(\tau) = O(\epsilon_f)$, $\bar{\mathbf{x}}_f(\mathbf{x}_{sr}, \tau) - \mathbf{x}_f(\tau) \to O(\epsilon_f)$. Hence, it follows that $\mathbf{x}_{sa}(\tau) - \mathbf{x}_s(\tau) = O(\epsilon_s + \epsilon_f)$, $\bar{\mathbf{x}}_f(\mathbf{x}_{sa}, \tau) - \mathbf{x}_f(\tau) \to O(\epsilon_s + \epsilon_f)$, which proves that (8) is an approximation of the full-order gearbox actuator model.

Appendix B. Nomenclature and model parameters

Table B.1
Servovalve variables and parameters

Name	Symbol	Value
Plunger position	x_v	m
Plunger speed	v_v	m/s
Electromagnetic force	f_e	N
Command current	i^*_e	A
User pressure (upstream pipeline pressure)	p_u	Pa
User flow (upstream pipeline oil flow)	q_u	m^3/s
Sensing chamber pressure	p_c	Pa
Supply pressure	p_s	50×10^5 Pa (T)
Discharge pressure	p_0	0 Pa (T)
Plunger mass	m_v	0.021 kg (T)
Spring stiffness	k_v	2700 N/m (T)
Spring pre-load	f_{v0}	−2.62 N (E)
Friction forces	$b_v(v_v)$	N (T)
Friction coefficient	b_v	6.0 N s/m (T)
Electro-mechanical constant	k_f	8.5 N/A (T)
Electro-magnetic time-constant	τ_e	10×10^{-3}s (T)
Dumping threshold displacement	x_{vd}	8.5×10^{-4} m (T)
Filling threshold displacement	x_{vf}	9.0×10^{-4} m (T)
Dumping and filling user port orifice areas	$A_d(x_v)$, $A_f(x_v)$	m^2 (T)
User port discharge coefficient	c_d	0.6 (T)
User port equivalent Bernoulli coefficient	c_{db}	0.32 (T)
User port number of orifices	n_o	2 (T)
Sensing chamber effective area	A_c	2.63×10^{-6} m^2 (T)
Sensing chamber cross-sectional area	A_{c0}	$3.0 \times 10^{-6}m^2$ (T)
Sensing chamber volume at $x_v = 0$	V_{c0}	$1.66 \times 10^{-8}m^3$ (T)
Number of capillary tubes of the sensing chamber	n_{oc}	4 (T)
Sensing capillary radius	r_{oc}	9×10^{-5} m (T)
Sensing capillary length	l_{oc}	2.6×10^{-3} m (T)
Sensing capillary conductance	g_c	1.7×10^{-13} m^3/(s Pa) (T)

Table B.2
Pipeline and oil parameters

Name	Symbol	Value
Oil density	ρ	852 kg/m^3 (T, @25 °C)
Oil dynamic viscosity	μ	240×10^{-3} Pa s (T, @25 °C)
Oil kinematic viscosity	ν	282×10^{-6} m^2/s (T, @25 °C)
Oil bulk modulus	β	600 MPa (T, @25 °C)
Pipeline radius	r_p	3.18×10^{-3} m (T)
Pipeline cross sectional area	A_p	31.7×10^{-6} m^2 (T)
Pipeline length	l_p	0.7 m (T)
Pipeline effective bulk modulus	$\beta_{e,p}$	52 MPa (T, @25 °C)
Frequency-dependent correction term for damping coefficient and natural frequency	α_p	1.04 (T)
Frequency-dependent correction term for damping coefficient and natural frequency	β_p	3.1 (T)

Table B.3
Gearbox actuator variables and parameters

Name	Symbol	Value
Downstream pipeline (outer chamber) pressure and internal chamber pressure ($k = 1,2$)	p_k, $p_{k,i}$	Pa
Downstream pipeline flow and tappet orifice flow ($k = 1,2$)	q_k, $q_{k,i}$	m^3/s
Position of piston, left and right hydraulic tappet	x_p, x_1, x_2	m
Speed of piston, left and right hydraulic tappet	v_p, v_1, v_2	m/s
Force applied by the gearbox devices to the piston	f_g	N
External tappet constraint	$\bar{x}_1$	-12.2×10^{-3} m (T)
External tappet constraint	$\bar{x}_2$	12.2×10^{-3} m (T)
disengaging threshold displacement	x_{D1}	-6.4×10^{-3} m (T)
disengaging threshold displacement	x_{D2}	6.4×10^{-3} m (T)
Synchronization threshold displacement	x_{S1}	-4.8×10^{-3} m (T)
Synchronization threshold displacement	x_{S2}	4.8×10^{-3} m (T)
Volume of the outer chamber for $x_k = 0$, $x_p = 0$ ($k = 1,2$)	V_{k0}	6.45×10^{-6} m^3 (T)
Volume of the inner chamber for $x_k = 0$, $x_p = 0$ ($k = 1,2$)	$V_{k,i0}$	1.86×10^{-6} m^3 (T)
Cross-sectional area of the outer chamber ($k = 1,2$)	A_k	5.54×10^{-4} m^2 (T)
Cross-sectional area of the inner chamber ($k = 1,2$)	$A_{k,i}$	2.1×10^{-4} m^2 (T)
Piston effective area	A_p	2.1×10^{-4} m^2 (T)
Tappet outer effective area	A_t	4.76×10^{-4} m^2 (T)
Tappet inner effective area	$A_{t,i}$	1.32×10^{-4} m^2 (T)
Tappet orifice conductance	g_{oa}	3.6×10^{-7} m^3/(s Pa) (T)
Piston mass	m_p	0.326 kg (T)
Tappet mass ($k = 1,2$)	m_k	0.062 kg (T)
Piston friction coefficient	b_{vp}	4500 Ns/m (T)
Tappet friction coefficient ($k = 1,2$)	b_{vk}	900 Ns/m (T)

Table B.4
Clutch actuator variables and parameters

Name	Symbol	Value
Pressure applied to the piston	$p_{c,p}$	Pa
Piston (release bearing) and plate displacements	x_{c1},x_{c2}	m
Axial constraint force	n_c	N
Transmissibility curve	$T_{cM}(n_c)$	Nm (T)
Piston mass	m_{c1}	0.75 kg (T)
Plate mass	m_{c2}	6.0 kg (T)
Piston cross-sectional area	$A_{c,p}$	665×10^{-6} m^2 (T)
Belville spring force and spring pre-load	$f_{c,b}(x_{c1}), f_{c0}$	N (E)
Belville coupling ratio	$c_r(x_{c1})$	(T)
Pre-load spring stiffness	k_c	N/m (E)
Friction forces	$b_{c1}(\dot{x}_{c1}), b_{c2}(\dot{x}_{c2})$	N (T)

Table B.5
Transmission shafts variables and parameters

Name	Symbol	Value
Engine speed	ω_e	rad/s
Total engine torque	T_e	Nm
Crankshaft output speed (flywheel-primary clutch disk) and main shaft input speed (secondary clutch disk)	ω_{c1}, ω_{c2}	rad/s
Main shaft output speed (gearbox primary shaft) and secondary shaft input speed (gearbox secondary shaft)	ω_{g1}, ω_{g2}	rad/s
Wheel speed	ω_w	rad/s
Crankshaft, main shaft and secondary shaft torsional displacement	θ_{ec}, θ_{cg}, θ_{gw}	rad
Crankshaft, main shaft and secondary shaft relative speed	ω_{ec}, ω_{cg}, ω_{gw}	rad/s
Crankshaft, main shaft and secondary shaft transmitted torque	T_{ec}, T_{cg}, T_{gw}	Nm
Transmitted clutch torque	T_c	Nm
Input and output gearbox torques (torques transmitted to the primary and secondary gearbox cogwheels)	T_{g1}, T_{g2}	Nm
Total wheel load torque	T_w	Nm
Actual speed ratio	r	
Equivalent engine inertia	J_e	0.159 kgm^2 (T)
Equivalent flywheel inertia	J_{c1}	0.0159 kgm^2 (T)
Equivalent clutch disk inertia	J_{c2}	0.0159 kgm^2 (T)
Equivalent gearbox primary shaft inertia	J_{g1}	0.039 kgm^2 (T)
Equivalent gearbox secondary shaft inertia	J_{g2}	0.039 kgm^2 (T)
Equivalent wheels, differential drive, tires and vehicle inertia	J_w	14.0 kgm^2 (T)
Crankshaft torsional stiffness	k_{ec}	32×10^3 Nm/rad (E)
Main shaft torsional stiffness	k_{cg}	3.2×10^3 Nm/rad (E)
Secondary shaft torsional stiffness	k_{gw}	16×10^3Nm/rad (E)
Crankshaft friction coefficient	b_{ec}	100 Nms/rad (E)
Main shaft friction coefficient	b_{cg}	4.0 Nms/rad (E)
Main shaft friction coefficient	b_g	0.012 Nms/rad (E)
Secondary shaft friction coefficient	b_{gw}	90 Nms/rad (E)
Gear ratios	r_1, r_2	{3.286,2.158} (T)
Force/torque gain during disengaging	k_{gD}	40 m^{-1} (E)
Torque/force gain during synchronization	k_{gS}	0.13 m (E)

References

[1] Schoner HP. Automotive mechatronics. Contr Eng Practice 2004;12 (11):1343–51.

[2] Link M, Vos B, Eggert E, Nasdal R. The automated shift transmission (AST) – possibilities and limits in production-type vehicles, SAE Paper 2001-01-0881 (2001).

[3] Wagner G. Application of transmission systems for different driveline configurations in passenger cars, SAE Paper 2001-01-0882 (2001).

[4] Wheals JC, Crewe C, Ramsbottom M, Rook S, Westby M. Automated manual transmissions – a European survey and proposed quality shift metrics, SAE Paper 2002-01-0929 (2002).

[5] Couderc P, Callenare J, Hagopian JD, Ferraris G. Vehicle driveline dynamic behaviour: Experimentation and simulation. J Sound Vib 1998;218 (1):133–57.

[6] Centea D, Rahnejat H, Menday MT. Non-linear multi-body dynamic analysis for the study of clutch torsional vibrations (judder). Appl Math Model 2001;25 (3):177–92.

[7] Montanari M, Ronchi F, Rossi C, Tilli A, Tonielli A. Control and performance evaluation of a clutch servo system with hydraulic actuation. Contr Eng Practice 2004;12 (11):1369–79.

[8] Fen L, Yuxuan L, Jianwu Z, Hongcheng H. Robust control for automated clutch of amt vehicle, SAE Paper 2002-01-0933 (2002).

[9] Lee H, Sul S, Cho H, Lee J. Advanced gear-shifting and clutching strategy for a parallel-hybrid vehicle. IEEE Ind Appl Mag 2000;6 (6):26–32.

[10] Pettersson M, Nielsen L. Gear shift by engine control. IEEE Trans Contr Syst Technol 2000;8 (3):495–507.

[11] Zanasi R, Visconti A, Sandoni G, Morselli R. Dynamic modeling and control of a car transmission system. In: Proc. IEEE/ASME Int. Conf. Advanced Intelligent Mechatronic, Vol. 1, Como (Italy), 8–12 July, 2001, p. 416–21.

[12] Bemporad A, Borodani P, Mannelli M. Hybrid control of an automotive robotized gearbox for reduction of consumptions and emissions. Lecture notes in computer science 2003;2623: 81–96.

[13] Fredriksson J, Egardt B. Nonlinear control applied to gearshifting in automated manual transmissions. In: Proc. 39th IEEE Conf. Decision Control, Sidney, Australia, 2000, p. 444–49.

[14] Garofalo F, Glielmo L, Iannelli L, Vasca F. Smooth engagement for automotive dry clutch. In: Proc. 40th IEEE Conf. Decision Control, Orlando, Florida, USA, 2001, p. 529–34.

[15] Lucente G, Montanari M, Rossi C. Modelling of a car driveline for servo-actuated gear-shift control, in: Proc. IEEE International Symposium on Industrial Electronics (ISIE 2005), Dubrovnik (Croatia), June 20–23, 2005.

[16] Merritt H. Hydraulic control systems. New York: Wiley; 1967.

[17] van der Schaft AJ, Schumacher H. Complementarity modeling of hybrid systems. IEEE Trans Automat Contr 1998;43 (4): 483–90.

[18] Yang WC, Tobler WE. Dissipative modal approximation of fluid transmission lines using linear friction model. ASME J Dyn Syst, Measurement, Control 1991;113 (1):152–62.

[19] Tunay I, Rodin E, Beck A. Modeling and robust control design for aircraft brake hydraulics. IEEE Trans Contr Syst Technol 2001;9 (2):319–29.

[20] Armstrong B, Dupont P, Canudas de Wit C. A survey of models, analysis tools and compensation methods for the control of machines with friction. Automatica 1994;30 (7):1083–138.

[21] Khalil HK. Nonlinear systems. Upper Saddle River, NJ: Prentice Hall; 1996.

[22] Zames G, Shneydor NA. Dither in nonlinear systems. IEEE Trans Automat Cont 1976;21 (5):660–7.

[23] Pervozvanski AA, Canudas de Wit C. Asymptotic analysis of the dither effect in systems with friction. Automatica 2002;38 (1):105–13.
[24] Iannelli L, Johansson KH, Jonsson UT, Vasca F. Averaging of nonsmooth systems using dither. Automatica 2006;42 (4):669–76.
[25] Krstic M, Wang H. Stability of extremum seeking feedback for general nonlinear dynamic systems. Automatica 2000;36 (4):595–601.
[26] Optimization toolbox user's guide. Natick (MA): The MathWorks, Inc., 2002.